Anatectic melt inclusions in ultra-high temperature granulites

Omar Gianola, Omar Bartoli, Bernardo Cesare, Fabio Ferri, Andrea Galli, Silvio Ferrero, Luca Capizzi, Christian Liebske, Laurent Remusat, Stefano Poli

Title: Anatectic melt inclusions in ultra-high temperature granulites

Omar Gianola[1], Omar Bartoli[1], Bernardo Cesare[1], Fabio Ferri[1], Andrea Galli[2], Silvio Ferrero[3], Luca Capizzi[1,4], Christian Liebske[2], Laurent Remusat[5], Stefano Poli[6]

[1] Dipartimento di Geoscienze, Università degli Studi di Padova, Via G. Gradenigo 6, 35131 Padova, Italy

[2] Institut für Geochemie und Petrologie, ETH Zürich, Switzerland

[3] Institut für Erd- und Umweltwissenschaften, Universität Potsdam, Potsdam, Germany

[4] Dipartimento di Scienze della Terra, Università degli Studi di Roma "La Sapienza", Roma, Italy

[5] Institut de Minéralogie, de Physique des Matériaux, et de Cosmochimie (IMPMC), UMR CNRS 7590 – Sorbonne Université – Muséum National d'Histoire Naturelle, Paris, France

[6] Dipartimento di Scienze della Terra "Ardito Desio", Università degli Studi di Milano, Milano, Italy

E-mail: omar.gianola@unipd.it

Key words: Fluid inclusions; Garnet; Granites; Gruf Complex; Nanogranitoids

Abstract

Partial melting up to ultra-high temperature (UHT) conditions is one of the major processes for the geochemical differentiation and reworking of the mid- to lower continental crust, with relevant implications on its rheological behaviour. UHT granulites from the Gruf Complex (Central Alps) display garnet and sapphirine porphyroblasts containing a variety of primary melt inclusions. Typically, melt inclusions in garnets occur as glassy and polycrystalline

inclusions (i.e. nanogranitoids), the latter often organized in mm-sized clusters associated with primary fluid inclusions. Nanogranitoids are characterized by an elliptical faceted shape, with variable sizes ranging from 2 to 115 μm, while glassy inclusions show negative crystal shapes that usually never exceed 15 μm in diameter and present CO_2-rich shrinkage bubbles. The characteristic mineral assemblage observed in nanogranitoids consists of quartz, biotite, muscovite, plagioclase, K-feldspar, kokchetavite and very rarely aluminosilicates. Glassy and re-homogenized melt inclusions are peraluminous and rhyolitic in composition, with SiO_2 = 69 – 80 wt% and $Na_2O + K_2O$ = 5 – 12 wt%. Commonly, the analysed melt inclusions have very high K_2O (> 6 wt%) and very low Na_2O (<2 wt%) contents, indicative for potassic to ultrapotassic melts. Measured H_2O contents of the melts range from 2.9 to 8.8 wt%, whereas CO_2 concentrations are between 160 and 1738 ppm. Accordingly, calculated viscosities for re-homogenized melt inclusions vary between 10^4 and 10^5 Pa·s. Related primary fluid inclusions mainly contain CO_2, with rare occurrence of CO and N_2, and are often associated with quartz, as well as different carbonates and phyllosilicates. It is assumed that the source for the carbonic fluid was external and probably related to the degassing lithospheric mantle. Consequently, it is argued that anatexis was initially triggered by incongruent dehydration melting reactions involving biotite breakdown and proceeded in the presence of an externally derived COH-bearing fluid. The coexistence of COH-bearing fluid and melt inclusions indicates that partial melting occurred under conditions of fluid-melt immiscibility. Potassic to ultrapotassic melt inclusions in UHT granulites suggests that lower crustal anatexis may play a stronger role in the redistribution of heat-producing elements (such as K_2O), potentially influencing the thermal structure of the continental crust.

1. INTRODUCTION

Buoyant andesitic continental crust (e.g. Rudnick, 1995; Taylor & McLennan, 1985) is a distinctive feature that differentiates the Earth from all the terrestrial planets of the Solar System. Although the upper levels of continents can be easily studied and sampled, the structure and chemical composition of the lower continental crust remain mostly enigmatic, due to its inaccessibility for direct observations. Rock xenoliths entrained in lavas and tectonically exposed metamorphic terranes, characterized by mineral assemblages that record lower crustal pressures (i.e. 5-15 kbar), are the only opportunities to obtain useful petrological information on the deep crust. A large number of such exposed terrains has provided a strong evidence that, on a regional scale, the lower continental crust can attain extreme thermal regimes (> 775 °C/GPa; e.g. Harley, 2008; Kelsey and Hand 2015; Brown and Johnson, 2018). Under these conditions, rocks are subjected to ultra-high temperature (UHT) metamorphism, in which peak temperatures exceed 900 °C at typical pressures of 7-13 kbar (Harley, 1998), with important implications for the geochemical differentiation, reworking and rheology of the lower crust (Brown, Korhonen, & Siddoway, 2011; Jamieson, Unsworth, Harris, Rosenberg, & Schulmann, 2011). UHT metamorphism is typically preserved in Mg-Al-rich metapelitic granulites (Brandt, Will, & Klemd, 2007; Harley, Hensen, & Sheraton, 1990; Harley, 2008; Kelsey, 2008; Santosh, Tsunogae, Li, & Liu, 2007), whose diagnostic paragenesis is characterized by the presence of sapphirine + quartz, Al-rich orthopyroxene + sillimanite and osumilite-bearing mineral assemblages (Harley, 1998; Kelsey, 2008). Progressing towards UHT conditions, the lower crust buffers the increasing temperature undergoing extensive partial melting, with the production of felsic magma that may then segregate from its source, leaving behind a more mafic and less fertile residuum (Clemens & Stevens 2016; Sawyer 1994; Sawyer, Cesare, & Brown, 2011; Vielzeuf & Holloway, 1988; White & Powell, 2002). Although S-type granites and granitic leucosomes are the two most prominent products of

crustal anatexis, they do not provide the pristine chemical composition of the felsic anatectic melt, because they are affected by fractional crystallization, crystal accumulation, chemical contamination and presence of xenocrysts (Carvalho, Sawyer, & Janasi 2016; Marchildon & Brown 2001; Milord, Sawyer, & Brown, 2001; Sawyer, 2008; Sawyer et al., 2011; Stevens, Villaros, & Moyen, 2007). Consequently, initial anatectic melt compositions have been mainly deduced from experimental studies (e.g. Clemens, Holloway, & White, 1986; Le Breton & Thompson, 1988; Montel & Vielzeuf, 1997; Stevens, Clemens, & Droop, 1997) and thermodynamic calculations (Grant, 2009; Holland & Powell, 2001; White, Stevens, & Johnson, 2011). Another compelling method to determine the composition of crustal melts during the early stages of anatexis is represented by primary melt inclusions entrapped in peritectic minerals during incongruent melting of metapelitic rocks (Acosta-Vigil, Cesare, London, & Morgan, 2007; Acosta-Vigil et al., 2016; Bartoli et al., 2013; Bartoli, Acosta-Vigil, Tajčmanová, Cesare, & Bodnar, 2016; Cesare, Marchesi, Hermann, & Gómez-Pugnaire, 2003; Cesare, Ferrero, Salvioli-Mariani, Pedron, & Cavallo, 2009; Ferrero et al., 2012; Ferrero, Wunder, Walczak, O'Brien, & Ziemann, 2015). Primary melt inclusions (MI) in high-grade metamorphic rocks typically show variable degrees of crystallization, ranging from glassy to fully crystallized, the latter also referred as *nanogranitoids* (Cesare, Acosta-Vigil, Bartoli, & Ferrero, 2015). Since MI represent droplets of early crustal melt, they preserve precious information on its primordial composition, before the melt is subjected to any chemical change due to magmatic differentiation.

At present, only very few studies have approached a detailed investigation of primary melt and fluid inclusions at UHT conditions (e.g. Cesare et al., 2009; Ferrero et al. 2012; Tacchetto et al., 2019) and therefore the pristine composition of anatectic melts and fluids in UHT rocks is largely unconstrained. In order to overcome this paucity, we report the occurrence of primary MI in peritectic minerals observed in UHT granulites of the Gruf Complex (Central Alps). The

aim of this study is to provide a microstructural framework and geochemical characterization of anatectic melts and fluids and evaluate their role during crustal reworking processes associated to UHT metamorphism.

2. GEOLOGICAL SETTING

The Penninic units of the Alpine nappe stack in the Central Alps are characterized by mineral isograds, isotherms and isobars that have a concentric shape, defining the so-called "Lepontine Metamorphic Dome" (Todd & Engi, 1997; Wenk, 1955). The Gruf Complex is a ~12 x 10 km migmatitic body between Switzerland and northern Italy, that is located in the south-eastern part of the Lepontine Dome (see Figure 1). To the west the Gruf Complex is delimited by the Adula Nappe, whereas to the north is surrounded by the ultramafic bodies of the Chiavenna Unit and by the crystalline rocks of the Tambo Nappe. To its eastern and southern margin, the Gruf Complex is intruded by the Bergell pluton, a tonalitic to granodioritic calc-alkaline intrusive body that formed between 33 and 30 Ma (Gianola et al., 2014; Oberli, Meier, Berger, Rosenberg, & Gieré, 2004; Samperton et al., 2015; von Blanckenburg, 1992). The southern extremity of the Gruf Complex, and part of the Bergell intrusion, are then cut by the 24 Ma old Novate granite (Liati, Gebauer, & Fanning, 2000), a strong peraluminous S-type granitic stock composed by a swarm of dykes that presumably derived from the partial melting of the surrounding gneissic units (von Blanckenburg, Früh-Green, Diethelm, & Stille, 1992). The dominant lithologies of the Gruf Complex are migmatitic orthogneisses, paragneisses and micaschists (Galli et al. 2011), which underwent upper amphibolite facies migmatisation (Bucher-Nurminen & Droop 1983; Nagel, De Capitani, & Frey, 2002) between 34 and 29 Ma (Galli et al. 2012). These rocks are also associated with irregular tabular bodies of charnockites and leucogranites (Galli et al. 2011). Both migmatitic orthogneisses and charnockites are characterized by the presence of rare sapphirine-bearing granulites, which mainly can be

observed as residual enclaves and schlieren (Galli et al. 2011). According to Galli et al. (2011), granulites and charnockites formed at ultra-high temperature conditions of T = 920-940 °C and P = 8.5-9.5 kbar, while migmatisation of the surrounding gneissic and metapelitic lithologies took place at ~740 °C and 6.5-7.5 kbar (Galli, Le Bayon, Schmidt, Burg, & Reusser, 2013).

3. ANALYTICAL TECHNIQUES AND EXPERIMENTAL METHODS

Back-scattered electron (BSE) images and semi-quantitative energy dispersive spectroscopy (EDS) analyses of MI were carried out with a CamScan MX2500 Scanning Electron Microscope (SEM), at the Department of Geosciences of the University of Padova (Italy).

Micro-Raman spectroscopy of MI was conducted with a HORIBA Jobin-Yvon LabRAM HR 800, equipped with a Nd:YAG laser (λ = 532 nm, laser power on sample ~2-3 mW), at the Institute of Earth and Environmental Science, University of Potsdam. Raman spectra were acquired between 100 and 4000 cm^{-1} with an acquisition time of 20 s during three spectral accumulations. The typical setup also included a grating of 300 lines/mm, a slit width of 100 µm and a confocal hole set at 200. Spectral resolution is considered to be of ~10 cm^{-1}, compared to available literature and databases.

The chemical composition of garnets was measured with a CAMECA SX50 microprobe, equipped with 4 wavelength dispersive spectrometers, at the C.N.R.-I.G.G. (Consiglio Nazionale delle Ricerche – Istituto di Geoscienze e Georisorse), Department of Geosciences, University of Padova. Analyses were carried out using a focussed beam with a current of 20 nA and an accelerating voltage of 15 kV. Counting times for each element were 10 s on peak and 5 s for the background.

Major element composition of glass and minerals in the re-homogenized and glassy MI were determined with a JEOL JXA 8200 microprobe at the Department of Earth Sciences

148 (University of Milano, Italy) employing an acceleration voltage of 15 kV, a beam current of 5
149 nA and beam diameter of 1 μm. Acquisition times were 10 s on peak and 5 s for background,
150 measuring Na and K first to avoid diffusional losses. Alkali concentrations were corrected
151 using conservative factors obtained by the analysis of hydrous and anhydrous leucogranitic
152 glasses of known composition. In particular, the standards employed in this study were a 10.1
153 wt% H_2O-bearing glass (LGB 2; Behrens & Jantos, 2001), a 5.5 wt% H_2O-bearing glass (DL;
154 Acosta-Vigil, London, Morgan, & Dewers, 2003) and a nearly anhydrous (H_2O = 300 ± 42
155 ppm) glass (B; Morgan & London, 2005).
156 Single garnet core and rim fragments (~1.5 x 2 mm in size), used for the re-homogenization
157 experiments of the nanogranitoids, were manually separated by cutting from 1.5 mm-thick
158 double-polished thick sections. Two sets of experiments were performed. In the first set, garnet
159 chips were charged into Au capsules (external diameter = 3 mm) alternating them with
160 powdered graphite (granulometry <45 μm). In the second type of experiments, the same gold
161 capsules were filled with alternating layers of garnet chips and powdered SiO_2, obtained from
162 tetraethylorthosilicate (TEOS). In both cases, capsules were crimped and sealed with an arc-
163 welder. Experiments with garnet + graphite charges were conducted using single-stage and
164 end-loaded piston cylinders at the Laboratory for Experimental Petrology, Department of Earth
165 Sciences, University of Milano. Capsules were placed vertically into MgO spacers and then
166 inserted in a NaCl sleeve-pyrex-graphite piston cylinder assembly. The temperature was
167 measured with a K-type (nickel-chromium / nickel-alumel) thermocouple, with an estimated
168 accuracy of ±5 °C and no corrections for the pressure effects on the electromotive force were
169 applied. Experiments were performed at 10 - 12 kbar (i.e. higher then the calculated peak
170 conditions, in order to prevent decrepitation of the inclusions) between 950 °C and 800 °C and
171 with variable run durations (1 to 10 hours). This allowed us to constrain the interval in which
172 re-homogenization was best attained. All runs were first pressurized to 10 - 12 kbar at room

temperature and then the assembly was isobarically heated at a constant heating rate (100 °C/min) until the targeted temperature was achieved. The experiments were terminated by switching off the power supply, resulting in quenching rates of ~40 °C/s. Capsules were then dissolved in aqua regia and the recovered garnets were singularly mounted in epoxy. Experiments with garnets + quartz charges were performed at the Institute of Geochemistry and Petrology, ETH Zurich, using single stage and end-loaded piston cylinders. The assembly consisted in a talc sleeve, pyrex (only for end-loaded piston cylinder), a graphite furnace and MgO spacers, in which the Au capsules were positioned. Temperature was measured with a B-type ($Pt_{94}Rh_6$ – $Pt_{70}Rh_{30}$) thermocouple. Experiments were performed at 12 kbar, 875 °C and with a duration of 10 h. The experimental procedure was the same used for the experiments with garnets + graphite charges. Although the two set of experiments have slightly different assemblies, it is assumed that this has no relevant influence on the re-homogenization of the inclusions.

H_2O and CO_2 contents of remelted inclusions were determined by Nano Secondary Ion Mass Spectrometry (NanoSIMS) employing a Cameca NanoSIMS 50 at Muséum National d'Histoire Naturelle of Paris, following the approaches of Bartoli, Cesare, Remusat, Acosta-Vigil, and Poli (2014) and Créon, Levresse, Remusat, Bureau, and Carrasco-Núñez (2018). Polished experimental capsules with quartz-garnet charges and standard glasses were mounted in indium, to lower the hydrogen background in the analysis chamber (Aubaud et al., 2007), and coated with gold (20 nm thick). Before each analysis, a 5 x 5 µm surface area was initially pre-sputtered for 150 s with a 170 pA primary Cs^+ rastering beam, in order to remove the gold coating and reach a sputtering steady-state (Thomen, Robert, & Remusat, 2014). Subsequently, the primary Cs^+ beam was set at 17 pA and scanned over a surface area of 3 x 3 µm. Nevertheless, to avoid surface contamination, only ions from the inner 1 x 1 µm region were collected with the "beam blanking mode". Exposed MI were analysed through collection of

198 secondary ions of $^{12}C^-$, $^{16}OH^-$, $^{28}Si^-$ and $^{56}Fe^{16}O^-$ in multicollection mode. Mass resolving power
199 was set at minimum 5500, enough to resolve interferences on $^{16}OH^-$. Each analysis consisted
200 in a stack of 200 cycles, with a duration of 1.024 s for every single cycle. The vacuum in the
201 analysis chamber never exceeded 2.5 x 10^{-10} Torr during the entire session of measurements.
202 H_2O and CO_2 contents of the glasses were quantified measuring $^{16}OH^-/^{28}Si^-$ and $^{12}C^-/^{28}Si^-$ ratios,
203 respectively (Bartoli et al., 2014, Créon et al., 2018). These ratios were converted into
204 concentrations using calibration curves obtained from standards of known composition.
205 Standards for the determination of H_2O included two standards used for the alkali correction
206 (DL and B, see above) plus an additional hydrous glass with 4.3 wt% H_2O (LGB1; Behrens &
207 Jantos, 2001). On the other hand, standards for CO_2 consisted in four trachyandesites (STR 9,
208 10, 11 and 13) from the Stromboli volcano, experimentally doped in carbon and water by
209 Bureau et al. (2003). Concentrations and uncertainties were calculated using the R program,
210 following the procedure described in Bartoli et al. (2014) and Thomen, Robert, & Remusat
211 (2014). Average major element and volatile concentrations of the analysed MI are reported in
212 Table 1.
213
214 ## 4. RESULTS
215
216 ### 4.1 Mineral assemblages of the UHT granulites
217 All the investigated samples were collected in the lower part of Val Codera, near the locality
218 of Bresciadega (see also Galli et al., 2011). Two varieties of UHT granulite with granofelsic
219 texture were studied (Figure 2). The first type corresponds to type A of Galli et al. (2011) and
220 consists in a dark, massive granulite containing large garnet (up to 2 cm) and sapphirine (up to
221 5 mm) porphyroblasts, associated with a matrix of up to 3 mm-sized orthopyroxene (Opx),
222 cordierite (Crd), biotite (Bt) and K-feldspar (Kfs). Garnet (Grt) appears as faint pink, rounded

crystals showing a clear zonation. Numerous mineral inclusions of biotite, orthopyroxene, sapphirine, plagioclase (Pl), cordierite, rutile (Rt), ilmenite, sillimanite, tourmaline, apatite (Ap), spinel, staurolite, corundum, monazite and zircon can be observed within the porphyroblastic garnets. On the other hand, sapphirine (Spr) is generally hypidiomorphic, prismatic and pleochroic (from pale-red to blue), showing sometimes a longitudinal, simple twinning system.

The second type of granulite belongs to type C of Galli et al. (2011). The rock is massive and melanocratic with a mineral assemblage made of porphyroblastic garnet (up to 1.5 cm), porphyroblastic orthopyroxene (<1.5 mm), biotite, cordierite, sillimanite and symplectitic spinel. Sapphirine may be present as symplectitic grains in the rock matrix, or as small (<500 μm) inclusions within garnet. Other mineral inclusions observed within garnet grains are: biotite, quartz, sillimanite, cordierite, plagioclase, spinel, zircon, apatite, corundum, rutile, staurolite and tourmaline.

In both granulites, melt inclusions (MI) are mainly present in the porphyroblastic garnets, where they may occur as single, scattered inclusions or may form mm-large clusters. These clusters are commonly found in the cores of the garnets (Figure 3a-b), but their occurrence towards to the rims has been also noticed (Figure 3c-d). The presence of different birefringent crystals under crossed polars (Figure 3e-f) indicates that the majority of MI are polycrystalline (i.e. nanogranitoids; Cesare et al. 2015). Often, fluid inclusions, usually showing a distinctive darker appearance and high birefringence (Figure 3g), occur associated to nanogranitoids within the same clusters. Moreover, sporadic glassy inclusions containing shrinkage bubbles have been also observed (Figure 3h). In contrast to polycrystalline MI, glassy MI occur exclusively as single inclusions dispersed in the garnets, without forming clusters, although occasionally, glassy MI may occur close to nanogranitoids. Moreover, rare MI with multiple birefringent phases have been also identified in sapphirine porphyroblasts of Type A granulites

(Figure 3i). The MI in sapphirine are too rare to allow their experimental re-melting, but were characterized by Raman spectroscopy.

4.2 Micro-Raman characterization of glassy, nanogranitoid and fluid inclusions

Micro-Raman investigations for the glassy inclusions observed in Type A samples show that the glass is hydrous (see Figure 4a). Furthermore, the single Raman band displayed at 1382 cm^{-1} (Figure 4a) indicates that some dissolved molecular CO_2 is also present in the melt (Brooker, Kohn, Holloway, McMillan & Carroll, 1999; Ni & Keppler 2013). Shrinkage bubbles in the glass contain CO_2, as demonstrated by the presence of the "Fermi-doublet" in the Raman spectra (see Figure 4a). Densities of CO_2 in these bubbles (see Table S1), calculated with the densimeter of Wang et al. (2011), range between 0.5 and 0.8 g/cm^3 (± 0.3 g/cm^3). Raman analyses showed that nanogranitoids (Figure 4b,c) may contain quartz, muscovite, phlogopite, K-feldspar, kokchetavite (a polymorph of $KAlSi_3O_8$) and an unknown phase with a main Raman peak at 430 cm^{-1}. Unexpectedly, Raman investigations also showed that some of these nanogranitoids could retain some CO_2 bubbles (Figure 4b,c), suggesting the existence of micropores. Nanogranitoids observed in sapphirine crystals from type A granulites (Figure 4d) contain quartz, muscovite, kokchetavite and the unknown phase with the peak at 430 cm^{-1}. Fluid inclusions (FI), present in both granulites, display a fluid fraction as well as a solid portion, in which several phases were identified. In type A granulites (together with CO_2) muscovite, Fe-magnesite, calcite, pyrophyllite, quartz and biotite were the most common phases. On the other hand, type C granulites have FI composed of – in addition to the same phases observed for type A – paragonite, magnesite, siderite, phlogopite, N_2 and CO (Figure 4e,f). For one inclusion it was possible to calculate the relative amount of components in the fluid, applying the method of Dubessy, Poty, and Ramboz (1989). The obtained molar fractions were 94 mol% for CO_2 and 6 mol% for N_2. For what concerns the carbonate phases, Fe-

magnesite in FI of both granulites has variable Fe content (Fe# = 100 x Fe/(Fe + Mg + Mn + Ca + Al), as defined by Boulard, Guyot, & Fiquet, 2012), typically ranging between Fe# = 20 and Fe# = 55. Calculated CO_2 densities (Wang et al. 2011) for FI in type A granulites vary between 0.3 and 1.0 g/cm^3 (see Table S1), a range comparable to that calculated for type C granulites (0.4-0.8 g/cm^3). It is also remarkable to notice that, neither in the shrinkage bubbles of glassy inclusions nor in fluid inclusions, H_2O was detected.

4.3 Microstructures of nanogranitoids

Detailed observations with SEM allowed to determine the principal microstructural features of nanogranitoids, as well as their mineral assemblage. Typically, MI of both Type A and C granulites have an elliptical faceted shape, with major axes ranging between 2 and 115 µm (Figure 5a-f). Nevertheless, for Type A, the size of MI decreases from rims to cores. MI in the rims have an average size of 47 ± 5 µm, those found in the intermediate region of the garnets (i.e. between cores and rims) are 35 ± 5 µm, while MI found in the cores have an average size of 24 ± 3 µm. Together with nanogranitoids with a nearly negative crystal shape (Figure 5a,b), some MI display natural decrepitation, with offshoots that are arranged radially around the inclusions (Figure 5c,d). The number of offshoots per inclusion varies drastically (from 1 to 10), with larger inclusions showing more (and usually longer) offshoots. The calculated average length of the offshoots for MI <45 µm in size is 6 µm, whereas MI bigger than 45 µm have an average length of the offshoots of 13 µm. Glassy inclusions in Type A granulites show negative crystal shapes and their size is <15 µm (average diameter: 8 µm). MI in type C granulites also have an elliptical faceted shape and show a polycrystalline nature. However, in contrast to MI in type A granulites, they have similar sizes from core to rim and hardly exceed 40 µm in diameter, with an average length of the major axis of 21 ± 2 µm. Also garnets from

297 type C granulites show some decrepitated MI (Figure 5e,f), which have an average length of
298 the offshoots of 5 μm.
299 In general, the mineral assemblage within nanogranitoids has an inequigranular and interlobate
300 fabric composed of mainly hypidiomorphic crystals of quartz, biotite, muscovite, plagioclase,
301 K-feldspar and very rarely aluminosilicates (Figure 5a-f). Sometimes nanogranitoids clearly
302 display an igneous microstructure defined by intergrowths of quartz, feldspars and biotite. SEM
303 analyses also highlighted the presence of accessory minerals, typically Cl-bearing apatite and
304 rutile, which are usually more idiomorphic compared to the other phases (Figure 5d,e).
305
306 **4.4 Chemical composition of host garnets and minerals in nanogranitoids**
307 In this section we report only chemical analyses of garnet porphyroblasts. For detailed chemical
308 analyses of all rock-forming minerals see Galli et al. (2011). Analysed garnets of Type A and
309 Type C granulites are almost pure almandine-pyrope solid solutions and display a zonation
310 marked by pyrope-richer rims (Type A = $Alm_{43-50}Prp_{44-53}Sps_{0-2}Grs_{2-6}$; Type C = $Alm_{44-54}Prp_{43-55}Sps_{0-1}Grs_{1-3}$) compared to cores (Type A = $Alm_{47-52}Prp_{39-48}Sps_{1-3}Grs_{3-9}$; Type C = $Alm_{50-62}Prp_{32-47}Sps_{0-1}Grs_{2-6}$).
313 For what concerns the nanogranitoids, their size often hampers a precise chemical
314 characterization of their mineral assemblage. Nevertheless, some nanogranitoid inclusions in
315 Type A granulites were large enough to allow the chemical analysis of the single mineral
316 phases (see Table S2). Plagioclases show variable X_{An} [An / (An + Ab)] between 0.10 (albite)
317 and 0.49 (andesine). By contrast, biotites are Ti-free and characterized by X_{Mg} [Mg / (Mg +
318 Fe^{2+})] ranging from 0.71 to 0.86. Other K-rich phases that have been recognized are K-feldspar
319 and phengite (Ph), the latter displaying a $X_{Mg} = 0.59$.
320
321

4.5 Remelted nanogranitoids

Experiments between 900 and 875 °C produced the most homogenized glasses. Remelted MI are typically <15 µm in size and display elongated to perfect negative crystal shapes (Figure 6a-d). Some inclusions, together with glass, display mineral phases like rutile and apatite that indent the walls of the MI (Figure 6c). These phases are interpreted to be accidental minerals trapped during the formation of the inclusions, since they are observed before and after the re-homogenization experiments. Therefore, they are not daughter minerals (i.e. phases that crystallized directly from the melt; e.g. Ferrero et al., 2012; Acosta-Vigil et al. 2016). Moreover, few MI may also exhibit bubbles (Figure 6d), suggesting that the fluid underwent incomplete dissolution in the melt during the experimental run or alternatively it diffused during cooling to form shrinkage bubbles (Lowenstern, 1995). A little fraction of the analysed MI population is characterized by the presence of unmelted daughter minerals, testifying incomplete remelting (Figure 6e,f). Typical daughter minerals coexisting with glass are euhedral to subhedral biotite grains (X_{Mg} = 0.82 – 0.88 and TiO_2 < 0.2 wt%, see Table S3) and rounded quartz crystals.

Experiments with garnets + quartz charges at 875 °C produced substantial amounts of melt in the matrix outside the garnets (Figure 6g), that infiltrated within the garnet crystals and led to the formation of large pockets of melt. These melt pockets differ microstructurally from remelted MI by their size (commonly >20 µm in diameter, although few of them have sizes comparable to remelted MI) and by the striking abundance of bubbles, a feature that indicates high fluid contents (Figure 6h). The matrix melt derives from the melting of mineral intergrowths or matrix phases, such as biotite and feldspar, which could not be avoided during the manual crushing of the garnet chips. Often, a peritectic reaction between the melt and the garnet can be observed, with the formation of orthopyroxene or corundum (Figure 6g).

346 Evidence of overheating in the MI has been observed at all temperatures, but predominantly at
347 950 °C. This is indicated by the formation of peritectic phases such as orthopyroxene or gedrite
348 (Figure 6i), by the recrystallization of new garnet within the inclusion or by a change in the
349 chemical composition of the garnet around the remelted inclusions. Chemical analyses (see
350 Table S3) for peritectic orthopyroxenes indicate that they are Al-rich (8.3 – 10.4 wt% at 950
351 °C and 6.5 – 9.2 wt% Al_2O_3 at lower temperature), with X_{Mg} = 0.69 - 0.73 (at 950 °C) and 0.67
352 – 0.84 (at 900-875 °C). These compositions are comparable to those measured in the
353 orthopyroxene porphyroblasts in the matrix of granulites (Galli et al. 2011). One analysis of a
354 recrystallized garnet 950 °C shows that the new garnet is Fe-poorer and Mg-richer (X_{Mg} = 0.64)
355 compared to the original garnet composition (X_{Mg} = 0.47). Since at 950 °C microstructural
356 evidence for overheating is dominant, the glasses analysed at these conditions were considered
357 not representative and therefore disregarded (Figure S1). For what concerns the experiments
358 performed at 800 °C, MI often display incomplete remelting and only rare homogeneous
359 glasses could be found. This might indicate that this temperature corresponds to the lower
360 boundary for remelting experiments.
361
362 **4.6 Chemical composition of glasses**
363 Figure 7a-b and Table S4 report chemical analyses of glasses for remelted inclusions and for
364 preserved glassy inclusions, all recalculated on anhydrous basis. For what concerns
365 experimentally remelted MI, analyses that displayed clear evidence for
366 contamination/interaction with the host garnet, or mixing with matrix melt, were discarded and
367 were not discussed (see Figure S1). Glasses are dominantly peraluminous (ASI = 1.0 – 1.6,
368 $[Al_2O_3/(CaO+Na_2O+K_2O)]_{molar}$), with only two MI that fall into the peralkaline field. Natural
369 glassy inclusions have a slightly more restricted range (ASI = 1.0 – 1.1) compared to re-
370 homogenized nanogranitoids. With rare exceptions, analysed MI are corundum-normative (Crn

371 = 0.2 – 4.88, see Table S4). Both re-homogenized MI and glassy inclusions are predominantly
372 rhyolitic in composition, with SiO_2 = 68.6 - 79.7 wt% and Na_2O+K_2O = 5.3 - 12.0 wt% (on
373 anhydrous basis), developing a negative correlated trend in the SiO_2 vs. Na_2O+K_2O space
374 (Figure 7b). However, melts with a trachytic composition have been also observed, as shown
375 by one MI from Type A granulite remelted at 875 °C. Glassy inclusions have slightly higher
376 total alkali contents compared to remelted nanogranitoids. Plotted in Harker variation diagrams
377 (Figure 8 a-f), glassy and re-homogenized inclusions show a clear increase in Al_2O_3 and K_2O
378 with decreasing SiO_2. By contrast, CaO, $FeO+MgO+TiO_2$, Na_2O and Cl display more scattered
379 distributions. Glassy inclusions differ from re-homogenized nanogranitoids by their low CaO
380 (<0.2 wt% vs. 0.2-2.0 wt%) and $FeO+MgO+TiO_2$ (<1.4 wt% vs. 1.4-3.4 wt%) concentrations.
381 All the analysed melt inclusions are characterized by a decoupling in the alkali content, with
382 most inclusions showing Na_2O concentrations <2 wt% and K_2O > 6 wt%. Re-homogenized MI
383 have variable K# ratios [K# = molar $K_2O/(K_2O+Na_2O)$ x100], ranging from 72 to 98 (average:
384 87 ± 4) for Type C granulites and from 56 to 82 (average: 71 ± 8) for Type A granulites.
385 Similarly, glassy inclusions from Type A granulites have K# between 59 and 87 (average: 77
386 ± 5).
387 H_2O and CO_2 concentrations of remelted inclusions, determined by NanoSIMS, are reported
388 in Table 2 and shown in Figure 9. H_2O contents in the analysed MI range from 2.9 to 8.8 wt%,
389 without any clear distinction between garnet cores and rims. Indeed, calculated averages are
390 6.2 ± 1.3 wt% (type A) and 7.1 ± 3.0 wt% (type C) for garnet cores, whereas for garnet rims is
391 4.4 ± 0.9 (type C). By contrast, CO_2 concentrations allow to subdivide the analysed MI into
392 two distinct families, one clustering at ~1200 ppm and the other showing concentrations <500
393 ppm. From Figure 9 it is also possible to notice that MI with low CO_2 concentrations are
394 characterized by a narrower range in H_2O (4.1 – 5.5 wt%) compared to MI with higher CO_2
395 contents.

396 # 5 DISCUSSION

397 ## 5.1 Anatexis at UHT conditions

398 The mineral assemblage displayed by nanogranitoid inclusions within the peritectic garnet of
399 the studied granulites indicates that these inclusions represent droplets of pristine felsic melt,
400 an observation that was also confirmed by the measurement of their chemical composition after
401 remelting experiments. Therefore, the investigated MI allow firstly an appraisal of the melting
402 regime on the regional scale and secondly, a better constraint on crustal anatexis under UHT
403 conditions.

404 Granulites from the Gruf Complex are characterized by the presence of glassy and
405 nanogranitoid inclusions. Their coexistence at the micrometric scale indicates that the melt
406 behaves differently when it is trapped within pores. Glassy inclusions are on average smaller
407 than nanogranitoids and therefore their preservation may be explained by inhibition of
408 crystallization (Cesare et al., 2009) due to the greater supersaturation required by smaller pores
409 to develop crystals compared to larger ones (Holness & Sawyer, 2008). Alternatively, lower
410 H_2O contents and, in turn, higher viscosities in some inclusions could have inhibited the
411 nucleation with the formation of glass (Bartoli, Acosta-Vigil, & Cesare, 2015). A different
412 volatile content in glassy and crystallized melt inclusions seems to be supported by the different
413 electron microprobe totals (Table 1). The chemical composition of re-homogenized MI is
414 consistent with the mineral assemblage observed in the nanogranitoids. This can be also
415 observed in the AKF diagram (Figure 10), where analysed glasses for Type A granulites plot
416 within the triangle defined by the tie-lines of the minerals measured in the non-remelted
417 nanogranitoids. Although the chemical composition of the minerals forming MI in Type C
418 granulites could not be measured (Figure 10b), it is assumed that the mineral assemblage should
419 be similar to the one noticed for Type A granulites and therefore an equivalent triangle for MI
420 in Type C granulites is expected. From Figure 10a it is also possible to observe that glassy

421 inclusions plot towards the K-apex of the triangle, while remelted MI tend to be more scattered,
422 with some analyses plotting slightly outside the triangle defined by the mineral assemblage. In
423 the Qz-Ab-Or normative diagram (see Figure S2) glassy and re-homogenized inclusions from
424 the Gruf Complex plot close to the Qz-Or join, considerably away from the haplogranite ternary
425 eutectic. Furthermore, MI also plot at lower Ab-contents compared to charnockites,
426 leucogranites and S- and A-type granites, but overlap the field displayed by MI from the Kerala
427 Khondalite Belt, consistent with their UHT nature.
428 Figure 8 shows that the analysed glasses have markedly different compositions compared to
429 the charnockites of the Gruf Complex, indicating that the charnockites might have been
430 generated from another metapelitic source or during a melting event unrelated with the
431 formation of the granulites. By contrast, MI have similar concentrations for CaO, Al_2O_3 and
432 FeO+MgO+TiO_2 compared to the leucogranites that intrude the migmatitic paragneisses and
433 micaschists (see Galli, Le Bayon, Schmidt, Burg, & Reusser, 2013). Moreover, MI overlap the
434 trend displayed by the melt inclusions from the Kerala Khondalite Belt (Cesare et al. 2009;
435 Ferrero et al. 2012), even though the latter have slightly higher FeO+MgO+TiO_2 and Cl
436 concentrations. On the other hand, MI from the Gruf Complex have different trends for
437 FeO+MgO+TiO_2, alkalis, and partly CaO, compared to A- and S-type granites. This evidence
438 strongly reinforces the assumption that S- and A-type granites do not mirror primary crustal
439 melts, but liquids modified by a large plethora of mechanisms during their production and
440 segregation from the source (see Introduction).
441 MI are characterized by high K_2O and low Na_2O concentrations compared to regional
442 charnockites and leucogranites, but also relative to A-and S-type granites (Figure 8d-e).
443 However, a decoupled behaviour in alkali contents has been also noticed in the MI from the
444 Kerala Khondalite Belt (KKB, S-India), in which ultrapotassic rhyolitic melts have been
445 reported (Cesare et al. 2009; Ferrero et al., 2012). It is generally believed that khondalites from

446 the KKB originated during crustal anatexis at UHT conditions (Nandakumar and Harley, 2000;
447 Yu, Santosh, Li, & Shaji, 2019) and therefore it seems that high K_2O/Na_2O ratios are a
448 distinctive feature of anatectic melts at extremely high crustal temperatures. K-rich melts have
449 also been experimentally derived by Patiño Douce and Johnston (1991) from a pelitic starting
450 material. In particular, their experiments between P = 7-13 kbar and T = 875-1075 °C give
451 K_2O-rich and Na_2O-poor liquids that closely resemble MI from the Gruf Complex and the
452 KKB. Additionally, Droop, Clemens, & Dalrymple (2003) obtained K-rich melts (K_2O/Na_2O
453 = 4.1 - 9.5) from partial melting experiments of metapelitic micaschists at 900 °C and 5 kbar.
454 In the AKF diagram (Figure 10) analyses for the KKB, as well as the experimental glasses of
455 Droop et al. (2003) and Patiño-Douce & Johnston (1991), plot towards the K-apex, overlapping
456 in part the field formed by the MI of the Gruf Complex. The fact that K-rich melts are observed
457 up to UHT conditions, independently of the pressure, may be explained by the role of titanium
458 in expanding the stability field of biotite towards higher temperatures. Consequently, the
459 melting of biotite may be delayed, compared to the melting of sodic plagioclase, leading to an
460 enrichment of potassium in the melt.
461 All this evidence suggests that melts produced at the onset of anatexis under high to ultra-high
462 temperature conditions are dominantly potassic to ultrapotassic, as was also recognized in
463 previous studies (Cesare et al., 2009; Ferrero et al., 2012).
464

465 **5.2 Volatiles in the deep crust**

466 Primary clusters of melt and fluid inclusions occur typically in both garnet cores and rims of
467 the granulites from the Gruf Complex, indicating that they were entrapped during the same
468 anatectic event. The coexistence of CO_2 with stepdaughter phases such as carbonates (Fe-
469 magnesite, siderite and calcite) and phyllosilicates (pyrophyllite, muscovite and biotite) within
470 FI strongly suggests that the original fluid had a COH(N) composition. Nevertheless, the

presence of K-rich phases such as muscovite and biotite might also indicate that some of the FI are instead mixed inclusions (fluid + melt) and therefore part of the H_2O may derive from the melt. Similar mixed inclusions were documented in garnet of crustal enclaves (Cesare, Maineri, Baron Toaldo, Pedron, & Acosta-Vigil, 2007) and anatectic granitoids (Ferrero, Braga, Berkesi, Cesare, & Laridhi Ouazaa, 2014). Although H_2O as a free phase has been never demonstrated by Raman spectroscopy within the measured FI of the Gruf Complex, its occurrence on the nanometric scale cannot be excluded (see also Lamadrid, Lamb, Santosh, & Bodnar, 2014; Esposito et al., 2016). On the other hand, carbonates and phyllosilicates are interpreted as re-speciation products after post-entrapment carbonation and hydration reactions between garnet host and fluid, as it has been suggested also for other HT/UHT terranes (Ferrero et al. 2014; Tacchetto et al., 2019; Carvalho et al., 2019). Hence, the different densities displayed by the FI are a direct consequence of incomplete reactions, which leave a variable amount of CO_2 in the residual fluid.

Raman spectroscopy measurements allowed to confirm the presence of CO_2 and H_2O in glassy and nanogranitoid inclusions (see Fig. 4), indicating that both inclusions derived from the similar melt. The ubiquity of pure CO_2-rich shrinkage bubbles (without any apparent detectable H_2O, see discussion above) within glassy inclusions can be explained by the preferential partition of H_2O into silicate melt than CO_2 (e.g. Holtz, Johannes, Tamic, & Behrens, 2001; Tamic, Behrens, & Holtz, 2001). Further investigations with NanoSIMS enabled the quantification of the minimum volatile component dissolved in this melt. The dissolved H_2O measured in the MI displays a wide spectrum (2.9-8.8 wt%), with a large proportions of the analyses that have >5 wt%. Such values indicate that crustal melts at T ~ 900 °C can have higher H_2O contents than commonly assumed for the haplogranitic system. However, as pointed out by Holtz et al. (2001), this behaviour is to be expected for melts that markedly differ from eutectic compositions and that involve the breakdown of micas in the melting

496 reaction, conditions which are both realised for the MI from the Gruf Complex. Moreover,
497 analogous H_2O contents have been also observed in MI from the granulites and upper
498 amphibolite-facies migmatites from the Strona Valley, in the Ivrea Zone (Carvalho et al.,
499 2019). It is therefore suggested that, at HT/UHT conditions, anatectic rhyolitic melts have
500 considerable but uneven H_2O contents, which may strongly affect the mobility of these
501 magmas. Variable water contents in anatectic melts were also recognized by Bartoli et al.
502 (2014) in peritectic garnets of amphibolite-facies migmatites close to the Ronda peridotite and
503 were interpreted to represent micro-scale buffered compositions due to heterogeneous domains
504 in the protholith. A similar mechanism might be envisaged also for the MI of the Gruf Complex,
505 since low and high values sometimes can be found in the same garnet crystal. Another striking
506 feature of the analysed MI is the marked difference in the CO_2 contents (Figure 9), with
507 inclusions forming two distinct groups. The highest CO_2 concentrations are nearly identical to
508 those observed in MI from granulites and amphibolites from the Ivrea Zone (see also Carvalho
509 et al., 2019), whereas the "CO_2-depleted" MI plot at lower values.
510 Our results clearly demonstrate that the peritectic garnets of the investigated UHT granulites
511 grew with coexisting COH-bearing fluids and silicate melts, that, due to the low solubility of
512 CO_2 in silicate melts (Holtz et al., 2001; Tamic et al., 2001), led to fluid-melt immiscibility.
513 The origin of the COH fluid in high-grade metamorphic rocks has been often source of debates.
514 The granulites from the Gruf Complex lack graphite in their mineral assemblage and therefore
515 an internal origin for carbon seems to be unlikely. However, the absence of graphite in the
516 rocks does not preclude the possibility that graphite was present in the original mineral
517 assemblage and was completely consumed before or during anatexis. Another source for
518 carbon may be represented by carbonaceous sediments interlayered in metapelitic rocks. In the
519 Gruf Complex very thin carbonate layers have been recognized only at the contact with the
520 ultramafic Chiavenna Unit, but never within the migmatitic gneisses that host the UHT

granulites and thus a sedimentary source for carbon does not seem a convincing argument. Accordingly, we infer that CO_2 was externally introduced in the lower crust, very likely from a mantle source. This is in agreement with previous studies that suggested the mantle as a common source for CO_2 in high temperature granulites (e.g. Hoefs & Touret, 1975; Jackson, Mattey, & Harris, 1988; Santosh & Omori, 2008; Touret & Huizenga, 2011). However, we also emphasize that without a rigorous isotopic determination for carbon, the origin of CO_2 remains uncertain. On the other hand, the minor N_2 amount detected in Type C granulites is interpreted to derive from the breakdown of NH_4^+-bearing micas during anatexis (e.g. Moin, Guillot, & Gibert, 1994; Cesare et al., 2007).

For the Gruf Complex, if an external source for CO_2 is assumed, the different CO_2 concentrations in the MI may be related to small-scale heterogeneities of the fluid composition within the matrix surrounding the growing peritectic garnets.

5.3 Rheology of anatectic melt

Granulites from the Gruf Complex represent UHT residues of metapelitic lower crustal rocks, attesting that substantial partial melting (~40 - 50%, Galli et al., 2011) occurred in the lowermost portions of the continental crust. This partial melting generated rhyolitic melts that are now preserved in the MI found in the peritectic garnets of the investigated granulites. An important aspect related to the genesis of anatectic rhyolitic melts is to determine some fundamental physical properties that govern the mobilization of these melts through the crust, such as viscosity and density. The complete analysis (geochemistry and water content) of four MI allowed us to calculate the viscosity of the melt. Assuming a temperature of 875 °C, which corresponds to the experimental temperature, and applying the equation of Scaillet, Holtz, Pichavant, & Schmidt (1996), viscosities vary between $10^{3.9}$ and $10^{4.5}$ Pa·s. These values are comparable to those calculated using the equation of Giordano, Russell, & Dingwell (2008),

546 which range between $10^{4.1}$ and $10^{4.8}$ Pa·s and are ~2 orders of magnitude lower than for
547 commonly assumed nearly anhydrous crustal melts at 900 °C. The calculated viscosities for
548 the melt during incipient UHT anatexis are consistent (within error) with the experimental
549 values obtained by Ardia, Giordano, and Schmidt (2008) for rhyolitic melts between 5 and 15
550 kbar at similar water contents (see Figure S3). Moreover, viscosities for MI from the Gruf
551 Complex overlap the range of viscosities obtained by Bartoli et al. (2013) for metatexites within
552 the metasedimentary sequence at the contact with the Ronda peridotite, in the Spanish Betic
553 Cordillera.
554 Combining viscosities with the respective densities allowed us to speculate on the ascent
555 velocity of the melt from its source. Our calculations were based on a simple porous flow model
556 (Turcotte & Schubert, 2002) and assuming an average density of 3.1 g/cm^3 for the lower crust
557 (Hacker, Kelemen, & Behn, 2015), a porosity of 8% (which corresponds to the liquid
558 percolation threshold of Vigneresse, Barbey, & Cuney, 1996) and a grain size for the matrix of
559 1-2 mm. For an average melt viscosity of $10^{4.4 \pm 0.3}$ Pa·s and an average density of 2.3 g/cm^3
560 (determined with the program DensityX by Iacovino and Till, 2019), melt velocities of 5-83
561 mm/year were calculated (see Table S5). Hence, if only porous flow is considered, at least tens
562 of thousands of years are needed before the melt will move at distances >1 km. At high melt
563 fractions it is expected that the pervasively distributed melt might be channelized by porosity
564 waves (e.g. Connolly & Podladchikov, 2015), resulting in an enhanced melt migration rate.
565 Furthermore, it has to be stressed that the calculated velocities are relative to a static solid
566 matrix. However, melting in the lower crust occurs in a dynamic environment, in which
567 deviatoric stresses may largely increase the ascent velocity of magmas (Sawyer 1994).
568 The Gruf Complex is as an example of upward extruded lower continental crust (Galli et al.
569 2012; Galli et al. 2013), that most probably was exhumed as a crustal diapir and for which an
570 exhumation rate of ~2 mm/year was estimated (Droop and Bucher-Nurminen, 1984). This

571 velocity is lower compared to those calculated for the anatectic melt and therefore it might be
572 plausible that the melt (or at least part of it) may have been effectively segregated from the
573 ascending migmatitic body. However, it is also expected that melts with physical properties
574 similar to those of the Gruf Complex may undergo less segregation if they are produced in
575 faster exhumed crustal sections. Field observations and numerical modelling (e.g. Ganguly,
576 Dasgupta, Cheng, & Neogi, 2000; Gerya, Perchuk, & Burg, 2008; Whitney, Teyssier, & Fayon,
577 2004) indicate that hot and partially molten crust may rise with velocities up to 50 mm/year,
578 i.e. in the range of those calculated in this study. Therefore, on the small scale, melts may
579 segregate from the source (forming leucosomes), but on the large scale they would probably
580 move coupled with the ascending hot crust (Teyssier & Whitney, 2002). Consequently,
581 segregation processes in migmatitic crustal domains should be evaluated also taking into
582 account the exhumation rate of the crust, and not only the ascent velocity of the melt. Although
583 the proposed approach might be simplistic, it gives a first-order approximation on the
584 ascending behaviour of pristine anatectic melts at the onset of crustal anatexis under UHT
585 regime.
586
587 ## 6. CONCLUSIONS
588 Evidence that the Earth's continental crust has the ability to attain, on a regional scale, ultra-
589 high temperatures has been widely reported. Under these conditions, middle and lower crust
590 undergo substantial modifications that have important consequences on their rheological
591 properties, which, in turn, may largely affect the mass transfer at the crust-mantle boundary.
592 Peraluminous, K-rich rhyolitic melt inclusions observed in garnet porphyroblasts of UHT
593 granulites from the Gruf Complex are the result of crustal anatexis, the latter driven by the
594 breakdown of biotite. The presence of primary melt and fluid inclusions with both a COH
595 volatile component suggests that anatexis initially started due to dehydration melting reactions

596 and was promoted by the influx of an external $CO_2 + H_2O$ fluid. Although the source of CO_2
597 cannot be undoubtedly ascertained, we infer that a mantle origin for the carbon is a more likely
598 explanation. On the other hand, the high H_2O content measured in the melt inclusions suggests
599 that anatectic melts at UHT conditions are less dry than commonly assumed, with relevant
600 implications for the viscosity of anatectic melts. The production of low density rhyolitic melts
601 in the lower crust may induce large-scale weakening (Rosenberg and Handy, 2005) that
602 ultimately may lead to the lateral flow of mountain belts (Jamieson et al. 2011) or to the
603 formation of domes and crustal diapirs (e.g. Gerya, Perchuk, Maresch, & Willner, 2004;
604 Teyssier & Whitney, 2002). The latter mechanism can be an effective geological process that
605 may trigger the exhumation of high-grade metamorphic rocks. Moreover, the potassic to
606 ultrapotassic composition of the analysed anatectic melts may indicate that crustal anatexis can
607 have a larger impact in the redistribution of heat-producing elements (such as K_2O), with
608 important implications for the thermal structure of the continental crust.
609 This study shows that anatectic melt inclusions provide a fundamental insight into the
610 comprehension of the melting regime in UHT terranes and the chemical differentiation of the
611 lower crust.
612
613 **ACKNOWLEDGEMENTS**
614
615 We thank Leonardo Tauro for the preparation of high quality polished thin sections, Raul
616 Carampin (University of Padova) and Andrea Risplendente (University di Milano) for their
617 help during electron microprobe analyses.
618 This research was supported by the Italian Ministry of Education, University, Research (Grant
619 SIR RBSI14Y7PF to O.B. and Grant PRIN 2017ZE49E7 to B.C.), the University of Padova

(research grant BART_SID19_01 to O.B.) and the CARIPARO (Cassa di Risparmio di Padova e Rovigo) project MAKEARTH (to F.F.).

The NanoSIMS facility at the Muséum National d'Histoire Naturelle in Paris was established by funds from the CNRS, Région Ile de France, Ministère délégué à l'Enseignement supérieur et à la Recherche, and the Muséum National d'Histoire Naturelle.

References

Acosta-Vigil, A., London, D., Morgan, G. B., & Dewers, T. A. (2003). Solubility of excess alumina in hydrous granitic melts in equilibrium with peraluminous minerals at 700–800 °C and 200 MPa, and applications of the aluminum saturation index. *Contributions to Mineralogy and Petrology*, *146*, 100-119.

Acosta-Vigil, A., Cesare, B., London, D., Morgan, G.B. (2007). Microstructures and composition of melt inclusions in a crustal anatectic environment, represented by metapelitic enclaves within El Hoyazo dacites, SE Spain. *Chemical Geology, 237*, 450-465.

Acosta-Vigil, A., Barich, A., Bartoli, O., Garrido, C.J., Cesare, B., Remusat, L., Poli, S., & Raepsaet, C. (2016). The composition of nanogranitoids in migmatites overlying the Ronda peridotites (Betic Cordillera, S Spain): the anatectic history of a polymetamorphic basement. *Contributions to Mineralogy and Petrology, 171,* 1-31.

Ardia, P., Giordano, D., & Schmidt, M. W. (2008). A model for the viscosity of rhyolite as a function of H_2O-content and pressure: A calibration based on centrifuge piston cylinder experiments. *Geochimica et Cosmochimica Acta*, *72*, 6103-6123.

643 Aubaud, C., Withers, A. C., Hirschmann, M. M., Guan, Y., Leshin, L. A., Mackwell, S. J., &
644 Bell, D. R. (2007). Intercalibration of FTIR and SIMS for hydrogen measurements in
645 glasses and nominally anhydrous minerals. *American Mineralogist*, *92*, 811–828.
646 Bartoli, O., Cesare, B., Poli, S., Bodnar, R.J., Acosta-Vigil, A., Frezzotti, M.L., & Meli, S.
647 (2013). Recovering the composition of melt and the fluid regime at the onset of
648 crustal anatexis and S-type granite formation. *Geology, 41,* 115-118.
649 Bartoli, O., Cesare, B., Remusat, L., Acosta-Vigil, A., & Poli, S. (2014). The H_2O content of
650 granite embryos. *Earth and Planetary Science Letters*, *395*, 281–290.
651 Bartoli, O., Acosta-Vigil, A., & Cesare, B. (2015). High-temperature metamorphism and
652 crustal melting: working with melt inclusions. *Periodico di Mineralogia*, *84*, 591-614.
653 Bartoli, O., Acosta-Vigil, A., Tajčmanová, L., Cesare, B., & Bodnar, R.J. (2016). Using
654 nanogranitoids and phase equilibria modeling to unravel anatexis in the crustal
655 footwall of the Ronda peridotites (Betic Cordillera, S Spain), *Lithos, 256-257,* 282-
656 299.
657 Behrens, H., & Jantos, N. (2001). The effect of anhydrous composition on water solubility in
658 granitic melts. *American Mineralogist*, *86*, 14-20.
659 Boulard, E., Guyot, F., & Fiquet, G. (2012). The influence on Fe content on Raman spectra and
660 unit cell parameters of magnesite-siderite solid solutions. *Physics and Chemistry of*
661 *Minerals*, *39*, 239-246.
662 Brandt, S., Will, T.M., Klemd, R. (2007). Magmatic loading in the proterozoic Epupa
663 Complex, NW Namibia, as evidenced by ultrahigh-temperature sapphirine-bearing
664 orthopyroxene-sillimanite-quartz granulites. *Precambrian Research, 153*, 143-178.
665 Brooker, R.A., Kohn, S.C., Holloway, J.R., McMillan, P.F., Carroll, M.R. (1999). Solubility,
666 speciation and dissolution mechanisms for CO_2 in melts on the $NaAlO_2$-SiO_2 join.
667 *Geochimica et Cosmochimica Acta*, *63*, 3549-3565.

668 Brown, M., Korhonen, F.J., Siddoway, C.S. (2011). Organizing melt flow through the crust.
669 *Elements, 7,* 261-266.
670 Brown, M., & Johnson, T. (2018). Secular change in metamorphism and the onset of global
671 plate tectonics. *American Mineralogist*, *103*, 181-196.
672 Bucher-Nurminen, K., & Droop, G. (1983). The metamorphic evolution of garnet-cordierite-
673 sillimanite-gneisses oft he Gruf-Complex, Eastern Pennine Alps. *Contributions to*
674 *Mineralogy and Petrology*, *84*, 215-227.
675 Buick, I. S., Stevens, G., & Gibson, R. L. (2004). The role of water retention in the anatexis of
676 metapelites in the Bushveld Complex Aureole, South Africa: an experimental study.
677 *Journal of Petrology*, *45*, 1777-1797.
678 Bureau, H., Trocellier, P., Shaw, C., Khodja, H., Bolfan-Casanova, N., & Demouchy, S.
679 (2003). Determination of the concentration of water dissolved in glasses and minerals
680 using nuclear microprobe. *Nuclear Instruments & Methods in Physics Research,*
681 *Section B: Beam Interactions with Materials and Atoms*, *210*, 449–454.
682 Carvalho, B. B., Sawyer, E. W., & Janasi, V. A. (2016). Crustal reworking in a shear zone:
683 Transformation of metagranite to migmatite. *Journal of Metamorphic Geology*, *34*,
684 237–264.
685 Carvalho, B.B., Bartoli, O., Ferri, F., Cesare, B., Ferrero, S., Remusat, L., Capizzi, L.S. & Poli,
686 S. 2019. Anatexis and fluid regime of the deep continental crust: New clues from melt
687 and fluid inclusions in metapelitic migmatites from Ivrea Zone (NW Italy). *Journal of*
688 *Metamorphic Geology*, *37*, 951-975.
689 Castro, N. A., de Araujo, C. E. G., Basei, M. A., Osako, L. S., Nutman, A. A., & Liu, D. (2012).
690 Ordovician A-type granitoid magmatism on the Ceará Central Domain, Borborema
691 Province, NE-Brazil. *Journal of South American Earth Sciences*, *36*, 18-31.

692 Cesare, B., Marchesi, C., Hermann, J., Gómez-Pugnaire, M.T. (2003). Primary melt
693 inclusions in andalusite from anatectic graphitic metapelites: implications for the
694 position of the Al_2SiO_5 triple point. *Geology, 31*, 573-576.
695 Cesare, B., Maineri, C., Baron Toaldo, A., Pedron, D., Acosta-Vigil, A. (2007). Immiscibility
696 between carbonic fluids and granitic melts during crustal anatexis: a fluid and melt
697 inclusion study in the enclaves of the Neogene Volcanic Province of SE Spain.
698 *Chemical Geology*, *237*, 433-449
699 Cesare, B., Ferrero, S., Salvioli-Mariani, E., Pedron, D., Cavallo, A. (2009). "Nanogranite"
700 and glassy inclusions: The anatectic melt in migmatites and granulites. *Geology, 37,*
701 627-630.
702 Cesare, B., Acosta-Vigil, A., Bartoli, O., & Ferrero, S., (2015). What can we learn from melt
703 inclusions in migmatites and granulites? *Lithos, 239*, 186-216.
704 Chappell, B. W., & White, A. J. R. (1992). I-and S-type granites in the Lachlan Fold Belt.
705 *Earth and Environmental Science Transactions of the Royal Society of Edinburgh*, *83*,
706 1-26.
707 Clemens, J.D., Holloway, J.R., White, A.J.R. (1986). Origin of an A-type granite: experimental
708 constraints. *American Mineralogist, 71,* 317-324.
709 Clemens, J.D., & Stevens, G. (2016). Melt segregation and magma interactions during crustal
710 melting: breaking out of the matrix. *Earth-Science Reviews, 160,* 333-349.
711 Clemens, J.D., & Watkins, J. M. (2001). The fluid regime of high-temperature metamorphism
712 during granitoid magma genesis. *Contributions to Mineralogy and Petrology*, *140*, 600-
713 606.
714 Connolly, J. A., & Podladchikov, Y. Y. (2015). An analytical solution for solitary porosity
715 waves: dynamic permeability and fluidization of nonlinear viscous and viscoplastic
716 rock. *Geofluids*, *15*, 269-292.

717 Créon, L., Levresse, G., Remusat, L., Bureau, H., & Carrasco-Núñez, G. (2018). New method
718 for initial composition determination of crystallized silicate melt inclusions. *Chemical*
719 *Geology*, *483*, 162–173.
720 de Almeida, C. N., de Pinho Guimarães, I., & da Silva Filho, A. F. (2002). A-type post-
721 collisional granites in the Borborema province-NE Brazil: The Queimadas pluton.
722 *Gondwana Research*, *5*, 667-681.
723 Droop, G. R., & Bucher-Nurminen, K. (1984). Reaction textures and metamorphic evolution
724 of sapphirine-bearing granulites from the Gruf Complex, Italian Central Alps. *Journal*
725 *of Petrology*, *25*, 766-803.
726 Droop, G. T. R., Clemens, J. D., & Dalrymple, D. J. (2003). Processes and conditions during
727 contact anatexis, melt escape and restite formation: the Huntly Gabbro Complex, NE
728 Scotland. *Journal of Petrology*, *44*, 995-1029.
729 Dubessy, J., Poty, B., & Ramboz, C. (1989). Advances in C-O-H-N-S fluid geochemistry based
730 on micro-Raman spectrometric analysis of fluid inclusions. *European Journal of*
731 *Mineralogy*, *1*, 517-534.
732 Esposito, R., Lamadrid, H. M., Redi, D., Steele-MacInnis, M., Bodnar, R. J., Manning, C. E.,
733 De Vivo, B., Cannatelli, C., & Lima, A. (2016). Detection of liquid H_2O in vapor
734 bubbles in reheated melt inclusions: Implications for magmatic fluid composition and
735 volatile budgets of magmas? *American Mineralogist*, *101*, 1691-1695.
736 Ferrero, S., Bartoli, O., Cesare, B., Salvioli-Mariani, E., Acosta-Vigil, A., Cavallo, A.,
737 Groppo, C., Battiston, S. (2012). Microstructures of melt inclusions in anatectic
738 metasedimentary rocks. *Journal of Metamorphic Geology, 30,* 303-322.
739 Ferrero, S., Braga, R., Berkesi, M., Cesare, B., & Laridhi Ouazaa, N. (2014). Production of
740 metaluminous melt during fluid-present anatexis: an example from the Maghrebian

741 basement, La Galite Archipelago, central Mediterranean. *Journal of Metamorphic*
742 *Geology*, *32*, 209-225.
743 Ferrero, S., Wunder, B., Walczak, K., O'Brien, P.J., Ziemann, M.A. (2015). Preserved near
744 ultrahigh-pressure melt from continental crust subducted to mantle depths.
745 *Geology, 43,* 447-450.
746 Florisbal, L. M., de Fátima Bitencourt, M., Nardi, L. V. S., & Conceição, R. V. (2009). Early
747 post-collisional granitic and coeval mafic magmatism of medium-to high-K tholeiitic
748 affinity within the Neoproterozoic Southern Brazilian Shear Belt. *Precambrian*
749 *Research*, *175*, 135-148.
750 Galli A., Le Bayon B., Schmidt M.W., Burg J.-P., Caddick M.J., Reusser E. (2011).
751 Granulites and charnockites of the Gruf Complex: Evidence for Permian ultra-high
752 temperature metamorphism in the Central Alps. *Lithos*, *124*, 17-45.
753 Galli, A., Le Bayon, B., Schmidt, M.W., Burg, J.-P., Reusser, E., Sergeev, S.A., Larionov, A.
754 (2012). U-Pb zircon dating of the Gruf Complex: disclosing the late Variscan granulitic
755 lower crust of Europe stranded in the Central Alps. *Contributions to Mineralogy and*
756 *Petrology, 163*, 353-378.
757 Galli, A., Le Bayon, B., Schmidt, M. W., Burg, J. P., & Reusser, E. (2013).
758 Tectonometamorphic history of the Gruf complex (Central Alps): exhumation of a
759 granulite–migmatite complex with the Bergell pluton. *Swiss Journal of Geosciences*,
760 *106*, 33-62.
761 Ganguly, J., Dasgupta, S., Cheng, W., & Neogi, S. (2000). Exhumation history of a section of
762 the Sikkim Himalayas, India: records in the metamorphic mineral equilibria and
763 compositional zoning of garnet. *Earth and Planetary Science Letters*, *183*, 471- 486.

764 Gerya, T. V., Perchuk, L. L., Maresch, W. V., & Willner, A. P. (2004). Inherent gravitational
765 instability of hot continental crust: Implications for doming and diapirism in granulite
766 facies terrains. *Special paper - Geological Society of America*, *380*, 97-116.
767 Gerya, T. V., Perchuk, L. L., & Burg, J. P. (2008). Transient hot channels: perpetrating and
768 regurgitating ultrahigh-pressure, high-temperature crust–mantle associations in
769 collision belts. *Lithos*, *103*, 236-256.
770 Ghani, A. A., Hazad, F. I., Jamil, A., Xiang, Q. L., Ismail, W. N. A. W., Chung, S. L., ... &
771 Mohd, M.R. (2014). Permian ultrafelsic A-type granite from Besar Islands group,
772 Johor, peninsular Malaysia. *Journal of Earth System Science*, *123*, 1857-1878.
773 Gianola, O., Schmidt, M.W., von Quadt, A., Peytcheva, I., Luraschi, P., Reusser, E. (2014).
774 Continuity in geochemistry and time of the Tertiary Bergell intrusion (Central Alps).
775 *Swiss Journal of Geosciences*, *107*, 197-222.
776 Giordano, D., Russell, J. K., & Dingwell, D. B. (2008). Viscosity of magmatic liquids: a model.
777 *Earth and Planetary Science Letters*, *271*, 123-134.
778 Goodenough, K. M., Upton, B. G. J., & Ellam, R. M. (2000). Geochemical evolution of the
779 Ivigtut granite, South Greenland: a fluorine-rich "A-type" intrusion. *Lithos*, *51*, 205-
780 221.
781 Grant, J.A. (2009). THERMOCALC and experimental modelling of melting of pelite, Morton
782 Pass, Wyoming. *Journal of metamorphic geology, 27,* 571-578.
783 Hacker, B. R., Kelemen, P. B., & Behn, M. D. (2015). Continental lower crust. *Annual Review*
784 *of Earth and Planetary Sciences*, *43*, 167-205.
785 Harley, S.L., Hensen, B.J., Sheraton, J.W. (1990). Two-stage decompression in orthopyroxene
786 –sillimanite granulites from Forefinger Point, Enderby Land, Antarctica: implications
787 for the evolution of the Archean Napier Complex. *Journal of metamorphic geology, 8,*
788 591-613.

789 Harley, S. L. (1998). On the occurrence and characterization of ultrahigh-temperature crustal
790 metamorphism. In: Treloar, P.J., O'Brian, P.J. (Eds.), What drives metamorphism and
791 metamorphic reactions? *Geological Society, London, Special Publications*, *138*, 81-107
792 Harley, S.L. (2008). Refining the P-T records of UHT crustal metamorphism. *Journal of*
793 *metamorphic geology, 26,* 125-154.
794 Hermann, J., & Spandler, C.J. (2008). Sediment melts at sub-arc depths: an experimental study.
795 *Journal of Petrology*, *49*, 717-740.
796 Hoefs, J., & Touret, J. (1975). Fluid inclusion and carbon isotope study from Bamble granulites
797 (South Norway). *Contributions to Mineralogy and Petrology*, *52*, 165-174.
798 Holland, T., & Powell, R. (2001). Calculation of phase relations involving haplogranitic melts
799 using an internally consistent thermodynamic dataset. *Journal of Petrology, 42,* 673-
800 683.
801 Holness, M. B., & Sawyer, E. W. (2008). On the pseudomorphing of melt-filled pores during
802 the crystallization of migmatites. *Journal of Petrology*, *49*, 1343-1363.
803 Holtz, F., Johannes, W., Tamic, N., & Behrens, H. (2001). Maximum and minimum water
804 contents of granitic melts generated in the crust: a reevaluation and implications. *Lithos*,
805 *56*, 1-14.
806 Iacovino, K., & Till, C. B. (2019). DensityX: A program for calculating the densities of
807 magmatic liquids up to 1,627° C and 30 kbar. *Volcanica*, *2*, 1-10.
808 Jackson, D. H., Mattey, D. P., & Harris, N. B. W. (1988). Carbon isotope compositions of fluid
809 inclusions in charnockites from southern India. *Nature*, *333*, 167.
810 Jamieson, R.A., Unsworth, M.J., Harris, N.B.W., Rosenberg, C.L., Schulmann, K. (2011).
811 Crustal melting and the flow of mountains. *Elements, 7,* 253-260.
812 Johannes, W., & Holtz, F. (1996). Petrogenesis and experimental petrology of granitic rocks.
813 Berlin Heidelberg: Springer-Verlag.

814 Jung, S., Hoernes, S., & Mezger, K. (2000). Geochronology and petrogenesis of Pan-African,
815 syn-tectonic, S-type and post-tectonic A-type granite (Namibia): products of melting of
816 crustal sources, fractional crystallization and wall rock entrainment. *Lithos*, *50*, 259-
817 287.
818 Kalsbeek, F., Jepsen, H. F., & Jones, K. A. (2001). Geochemistry and petrogenesis of S-type
819 granites in the East Greenland Caledonides. *Lithos*, *57*, 91-109.
820 Kelsey, D.E. (2008). On ultrahigh-temperature crustal metamorphism. *Gondwana Research,*
821 *13,* 1-29.
822 Kelsey, D.E., Hand, M. (2015). On ultrahigh temperature crustal metamorphism: phase
823 equilibria, trace element thermometry, bulk composition, heat sources, timescales and
824 tectonic settings. *Geoscience Frontiers, 6,* 311-356.
825 King, P. L., White, A. J. R., Chappell, B. W., & Allen, C. M. (1997). Characterization and
826 origin of aluminous A-type granites from the Lachlan Fold Belt, southeastern Australia.
827 *Journal of Petrology*, *38*, 371-391.
828 King, P. L., Chappell, B. W., Allen, C. M., & White, A. J. R. (2001). Are A-type granites the
829 high-temperature felsic granites? Evidence from fractionated granites of the Wangrah
830 Suite. *Australian Journal of Earth Sciences*, *48*, 501-514.
831 Lamadrid, H. M., Lamb, W. M., Santosh, M., & Bodnar, R. J. (2014). Raman spectroscopic
832 characterization of H_2O in CO_2-rich fluid inclusions in granulite facies metamorphic
833 rocks. *Gondwana Research*, *26*, 301-310.
834 Le Breton, N., Thompson, A.B. (1988). Fluid-absent (dehydration) melting of biotite in
835 metapelites in the early stages of crustal anatexis. *Contributions to Mineralogy and*
836 *Petrology, 99,* 226-237.
837 Liati, A., Gebauer, D., & Fanning, M. (2000). U-Pb SHRIMP dating of zircon from the

838 Novate granite (Bergell, Central Alps): evidence for Oligocene-Miocene magmatism,
839 Jurassic/Cretaceous continental rifting and opening of the Valais trough.
840 *Schweizerische Mineralogische und Petrographische Mitteilungen*, *80*, 305-316.

841 Lowenstern, J. B. (1995). Applications of silicate-melt inclusions to the study of magmatic
842 volatiles. *Magmas, Fluids, and Ore Deposits*, *23*, 71–99.

843 Marchildon, N., Brown M. (2001). Melt segregation in late syn-tectonic anatectic migmatites:
844 an example from the Onawa contact aureole, Maine, USA. *Physics and Chemistry of*
845 *the Earth, Part A: Solid Earth and Geodesy, 26,* 225-229.

846 McDermott, F., Harris, N. B. W., & Hawkesworth, C. J. (2000). Geochemical constraints on
847 the petrogenesis of Pan-African A-type granites in the Damara Belt, Namibia. *Henno*
848 *Martin Commemorative Volume: Communications of the Geological Survey of*
849 *Namibia, Special Publication of the Geol. Survey of Namibia*, *12*, 139-148.

850 Milord, I., Sawyer, E.W., Brown, M. (2001). Formation of diatexite migmatite and granite
851 magma during anatexis of semi-pelitic metasedimentary rocks: an example from St.
852 Malo, France. *Journal of Petrology, 42,* 487-505.

853 Moin, B., Guillot, C., & Gibert, F. (1994). Controls of the composition of nitrogen-rich fluids
854 originating from reaction with graphite and ammonium-bearing biotite. *Geochimica et*
855 *Cosmochimica Acta*, *58*, 5503-5523.

856 Montel, J-M., Vielzeuf, D. (1997). Partial melting of metagreywackes, part II. Compositions
857 of minerals and melts. *Contributions to Mineralogy and Petrology, 128,* 176-196.

858 Morgan, G. B., & London, D. (2005). Effect of current density on the electron microprobe
859 analysis of alkali aluminosilicate glasses. *American Mineralogist*, *90*, 1131-1138.

860 Nagel, T., De Capitani, C., Frey, M. (2002). Isograds and P-T evolution in the eastern
861 Lepontine Alps (Graubünden, Switzerland). *Journal of Metamorphic Geology*, *20*, 309-
862 324.

Nandakumar, V., & Harley, S. L. (2000). A reappraisal of the pressure-temperature path of granulites from the Kerala Khondalite Belt, southern India. *The Journal of Geology*, *108*, 687-703.

Ni, H., Keppler, H. (2013). Carbon in silicate melts. *Reviews in Mineralogy & Geochemistry*, *75*, 251-287.

Oberli, F., Meier, M., Berger, A., Rosenberg, C.L., & Gieré, R. (2004). U-Th-Pb and $^{230}Th/^{238}U$ disequilibrium isotope systematics: Precise accessory mineral chronology and melt evolution tracing in the Alpine Bergell intrusion. *Geochimica et Cosmochimica Acta*, *68*, 2543-2560.

Patiño Douce, A. E., & Johnston, A. D. (1991). Phase equilibria and melt productivity in the pelitic system: implications for the origin of peraluminous granitoids and aluminous granulites. *Contributions to Mineralogy and Petrology*, *107*, 202-218.

Rosenberg, C. L., & Handy, M. R. (2005). Experimental deformation of partially melted granite revisited: implications for the continental crust. *Journal of metamorphic Geology*, *23*, 19-28.

Samperton, K.M., Schoene, B., Cottle, J.M., Keller, C.B., Crowley, J.L., Schmitz, M.D. (2015). Magma emplacement, differentiation and cooling in the middle crust: integrated zircon geochronological-geochemical constraints from the Bergell intrusion, Central Alps. *Chemical Geology*, *417*, 322-340.

Santosh, M., Tsunogae, T., Li, J.H., Liu, S.J. (2007). Discovery of sapphirine-bearing Mg-Al granulites in the North China Craton: implications for Paleoproterozoic ultrahigh temperature metamorphism. *Gondwana Research*, *11*, 263-285.

Santosh, M., & Omori, S. (2008). CO_2 flushing: a plate tectonic perspective. *Gondwana Research*, *13*, 86-102.

Sawyer, E.W. (1994). Melt segregation in the continental crust. *Geology*, *22*, 1019-1022.

888 Sawyer, E.W. (2008). *Atlas of migmatites*. The Canadian Mineralogist Special Publication 9.
889 Quebec: Mineralogical Association of Canada; Ottawa: NRC Research Press.
890 Sawyer, E.W., Cesare, B., Brown M. (2011). When the continental crust melts. *Elements, 7,*
891 229-234.
892 Scaillet, B., Holtz, F., Pichavant, M., & Schmidt, M. (1996). Viscosity of Himalayan
893 leucogranites: Implications for mechanisms of granitic magma ascent. *Journal of*
894 *Geophysical Research: Solid Earth*, *101*, 27691-27699.
895 Schmidt, M. W. (2015). Melting of pelitic sediments at subarc depths: 2. Melt chemistry,
896 viscosities and a parameterization of melt composition. *Chemical Geology*, *404*, 168-
897 182.
898 Stevens, G., Clemens, J.D., Droop, G.T.R. (1997). Melt production during granulite-facies
899 anatexis: experimental data from "primitive" metasedimentary protholiths.
900 *Contributions to Mineralogy and Petrology, 128,* 352-370.
901 Stevens, G., Villaros, A., Moyen, J-F. (2007). Selective peritectic garnet entrainment as the
902 origin of geochemical diversity in S-type granites. *Geology, 35,* 9-12.
903 Rudnick, R.L. (1995). Making continental crust. *Nature, 378,* 571-578.
904 Tacchetto, T., Bartoli, O., Cesare, B., Berkesi, M., Aradi, L. E., Dumond, G., & Szabó, C.
905 (2019). Multiphase inclusions in peritectic garnet from granulites of the Athabasca
906 granulite terrane (Canada): Evidence of carbon recycling during Neoarchean crustal
907 melting. *Chemical Geology*, *508*, 197-209.
908 Tamic, N., Behrens, H., & Holtz, F. (2001). The solubility of H_2O and CO_2 in rhyolitic melts
909 in equilibrium with a mixed CO_2–H_2O fluid phase. *Chemical geology*, *174*, 333-347.
910 Taylor, S.R., McLennan, S.M. (1995). The geochemical evolution of the continental crust.
911 *Reviews of Geophysics*, *33*, 241-265.
912 Teyssier, C., & Whitney, D. L. (2002). Gneiss domes and orogeny. *Geology*, *30*, 1139-1142.

913

914 Thomen, A., Robert, F., & Remusat, L. (2014). Determination of the nitrogen abundance in
915 organic materials by NanoSIMS quantitative imaging. *Journal of Analytical Atomic*
916 *Spectrometry*, *29*, 512–519.

917 Todd, C.S., Engi, M. (1997). Metamorphic field gradients in the Central Alps. *Journal of*
918 *metamorphic geology*, *15*, 513-530.

919 Touret, J. L., & Huizenga, J. M. (2011). Fluids in granulites. *Geological Society of America*
920 *Memoirs*, *207*, 25-37.

921 Trommsdorff, V., & Nievergelt, P. (1983). The Bregaglia (Bergell) Iorio intrusive and its field
922 relations. *Memorie della Società Geologica Italiana*, *26*, 55-68.

923 Tulloch, A. J., Ramezani, J., Kimbrough, D. L., Faure, K., & Allibone, A. H. (2009). U-Pb
924 geochronology of mid-Paleozoic plutonism in western New Zealand: Implications for
925 S-type granite generation and growth of the east Gondwana margin. *Geological Society*
926 *of America Bulletin*, *121*, 1236-1261.

927 Turcotte, D., & Schubert, G. (2014). Geodynamics. Cambridge university press.

928 Vielzeuf, D., Holloway, J.R. (1988). Experimental determination of the fluid-absent melting
929 relations in the pelitic system. *Contributions to Mineralogy and Petrology, 98,* 257-
930 276.

931 Vigneresse, J. L., Barbey, P., & Cuney, M. (1996). Rheological transitions during partial
932 melting and crystallization with application to felsic magma segregation and transfer.
933 *Journal of Petrology*, *37*, 1579-1600.

934 Visonà, D., & Lombardo, B. (2002). Two-mica and tourmaline leucogranites from the Everest–
935 Makalu region (Nepal–Tibet). Himalayan leucogranite genesis by isobaric heating?
936 *Lithos*, *62*, 125-150.

937 Von Blanckenburg, F. (1992). Combined high-precision chronometry and geochemical

938 tracing using accessory minerals: Applied to the Central-Alpine Bergell intrusion
939 (Central Europe). *Chemical Geology*, *100*, 19-40.

940 Von Blanckenburg, F., Früh-Green, G., Diethelm, K., & Stille, P. (1992). Nd-, Sr-, O-
941 isotopic and chemical evidence for a two-stage contamination history of mantle magma
942 in the Central-Alpine Bergell intrusion. *Contributions to Mineralogy and Petrology*,
943 *110*, 33-45.

944 Wang, X., Ming Chou, I., Hu, W., Burruss, R.C., Sun, Q., & Song Y. (2011). Raman
945 spectroscopic measurements of CO_2 density: experimental calibration with high-
946 pressure optical cell (HPOC) and fused silica capillary capsule (FSCC) with application
947 to fluid inclusion observations. *Geochimica et Cosmochimica Acta*, *75*, 4080-4093.

948 Wenk, E., (1955). Eine Strukturkarte der Tessineralpen. *Schweizerische und Mineralogische*
949 *und Petrographische Mitteilungen*, *35*, 311-319.

950 Whalen, J. B., Currie, K. L., & Chappell, B. W. (1987). A-type granites: geochemical
951 characteristics, discrimination and petrogenesis. *Contributions to Mineralogy and*
952 *Petrology*, *95*, 407-419.

953 White, R.W., Powell, R. (2002). Melt loss and the preservation of granulite facies material
954 assemblages. *Journal of metamorphic geology, 20,* 621-632.

955 White, R.W., Stevens, G., Johnson, T.E. (2011). Is the crucible reproducible? Reconciling
956 melting experiments with thermodynamic calculations. *Elements, 7*, 241-246.

957 Whitney, D. L., Teyssier, C., & Fayon, A. K. (2004). Isothermal decompression, partial melting
958 and exhumation of deep continental crust. *Geological Society, London, Special*
959 *Publications*, *227*, 313-326.

960 Yu, B., Santosh, M., Li, S. S., & Shaji, E. (2019). Petrology, phase equilibria modelling, and
961 in situ zircon and monazite geochronology of ultrahigh-temperature granulites from the
962 khondalite belt of southern India. *Lithos*, *348-349*, 105195.
963 Zhang, H. F., Parrish, R., Zhang, L., Xu, W. C., Yuan, H. L., Gao, S., & Crowley, Q. G. (2007).
964 A-type granite and adakitic magmatism association in Songpan–Garze fold belt, eastern
965 Tibetan Plateau: implication for lithospheric delamination. *Lithos*, *97*, 323-335.
966
967
968
969
970
971
972
973
974
975
976
977
978
979
980
981
982
983
984

985

986

987

	Type A granulites		Type C granulites	
	BRE-core	**BRE-rim (glassy)**	**GRAG-core**	**GRAG-rim**
No. analyses by EPMA[a] / NanoSIMS	6 / 6	11	21 / 3	6 / 7
Wt%				
SiO_2	70.08 (2.51)	75.33 (1.26)	74.90 (1.00)	71.93 (1.54)
TiO_2	0.05 (0.04)	0.00 (0.01)	0.05 (0.04)	0.06 (0.07)
Al_2O_3	14.45 (0.88)	12.87 (0.64)	11.75 (0.43)	13.29 (1.19)
FeO	1.67 (0.32)	0.91 (0.05)	1.52 (0.14)	1.93 (0.36)
MnO	0.05 (0.02)	0.05 (0.02)	0.02 (0.02)	0.08 (0.04)
MgO	0.54 (0.24)	0.10 (0.08)	0.71 (0.10)	0.53 (0.23)
CaO	0.94 (0.55)	0.05 (0.02)	0.51 (0.15)	0.55 (0.19)
Na_2O	1.96 (0.54)	1.66 (0.38)	0.73 (0.27)	0.72 (0.39)
K_2O	7.31 (1.43)	8.67 (0.82)	6.96 (0.48)	7.95 (1.88)
P_2O_5	0.20 (0.18)	0.04 (0.03)	0.12 (0.06)	0.17 (0.15)
Cl	0.04 (0.03)	0.01 (0.00)	0.06 (0.02)	0.12 (0.04)
Total	97.31 (2.33)	99.70 (0.31)	97.33 (0.79)	97.33 (1.57)
H_2O by NanoSIMS [wt%]	6.20 (1.25)	-	7.05 (3.00)	4.35 (0.92)
CO_2 by NanoSIMS [ppm]	779 (326)	-	1113 (843)	940 (407)
ASI	1.14 (0.13)	1.06 (0.03)	1.24 (0.07)	1.27 (0.19)
K#	71 (8)	77 (5)	87 (4)	87 (7)
Mg#	35 (8)	13 (8)	44 (4)	32 (11)
CIPW norm				
Quartz	27.04	31.56	40.98	34.15
Corundum	2.10	0.76	2.39	2.89
Orthoclase	43.23	51.23	41.13	46.98
Albite	16.59	14.02	6.16	6.13
Anorthite	3.31	0.00	1.73	1.65
Hypersthene	4.43	2.01	4.51	4.91
Ilmenite	0.10	0.01	0.09	0.11
Apatite	0.47	0.10	0.29	0.39

[a] EPMA = electron probe micro-analyzer

988

989 **TABLE 1** Average compositions of remelted and preserved glassy MI. Numbers in parentheses
990 refer to the standard error of the mean expressed as 2σ. ASI = molar
991 [Al_2O_3/(CaO+Na_2O+K_2O)], K# = molar [K_2O/(K_2O+Na_2O)] x 100; Mg# = molar
992 [MgO/(MgO+FeO)] x 100.

Analysis	Sample	Approx. size	Homogeneity	H_2O [wt%]	1σ error	CO_2 [ppm]	1σ error
Type A granulites							
C_MI1_Gr1	BRE17-B13 core	<10 µm	Glass	5.52	0.04	460	20
C_MI3_Gr3_1	BRE17-B13 core	≥ 20 µm	Glass + bubble	8.27	0.27	1164	33
C_MI3_Gr3_2	BRE17-B13 core	≥ 20 µm	Glass + bubble	7.34	0.23	1064	31
C_MI16_Gr4	BRE17-B13 core	≥ 20 µm	Glass + 10% crystals + bubble	6.88	0.21	1194	34
E_MI6_Gr2_1	BRE17-D2 core	<10 µm	Glass	4.41	0.04	408	17
E_MI6_Gr2_2	BRE17-D2 core	<10 µm	Glass	4.76	0.04	387	17
OG16_MI2_Gr1	BRE17-B13 rim	<10 µm	Glass + 3% crystals	4.68	0.04	1153	32
Type C granulites							
A_MI1_Gr1	GRAG-P3 core	<10 µm	Glass	8.75	0.07	1738	41
A_MI3_Gr2	GRAG-P3 core	<10 µm	Glass + bubble	8.34	0.06	1291	33
A_MI2_Gr2	GRAG-P3 core	<10 µm	Glass + 3% crystals	4.06	0.04	310	17
F_MI12_Gr1	GRAG-P2 Gr1 rim	10 - 20 µm	Glass + 3% crystals	4.51	0.04	160	15
F_MI1_Gr4	GRAG-P2 Gr1 rim	<10 µm	Glass + 2% crystals	2.88	0.04	1569	34
OG18_MI1_Gr4	GRAG-P3 rim	<10 µm	Glass	3.11	0.04	1149	28
OG18_MI3_Gr4	GRAG-P3 rim	<10 µm	Glass	3.44	0.04	1064	32
OG18_MI6_Gr1	GRAG-P3 rim	<10 µm	Glass + 1% crystals	5.18	0.04	221	15
OG18_MI4_Gr2_1	GRAG-P3 rim	10 - 20 µm	Glass	5.94	0.04	1287	31
OG18_MI4_Gr2_2	GRAG-P3 rim	10 - 20 µm	Glass	5.41	0.04	1132	27

993

994 **TABLE 2** H_2O and CO_2 contents of re-homogenized MI determined by NanoSIMS.

995

996

997

998

999

1000

1001

FIGURES TEXT

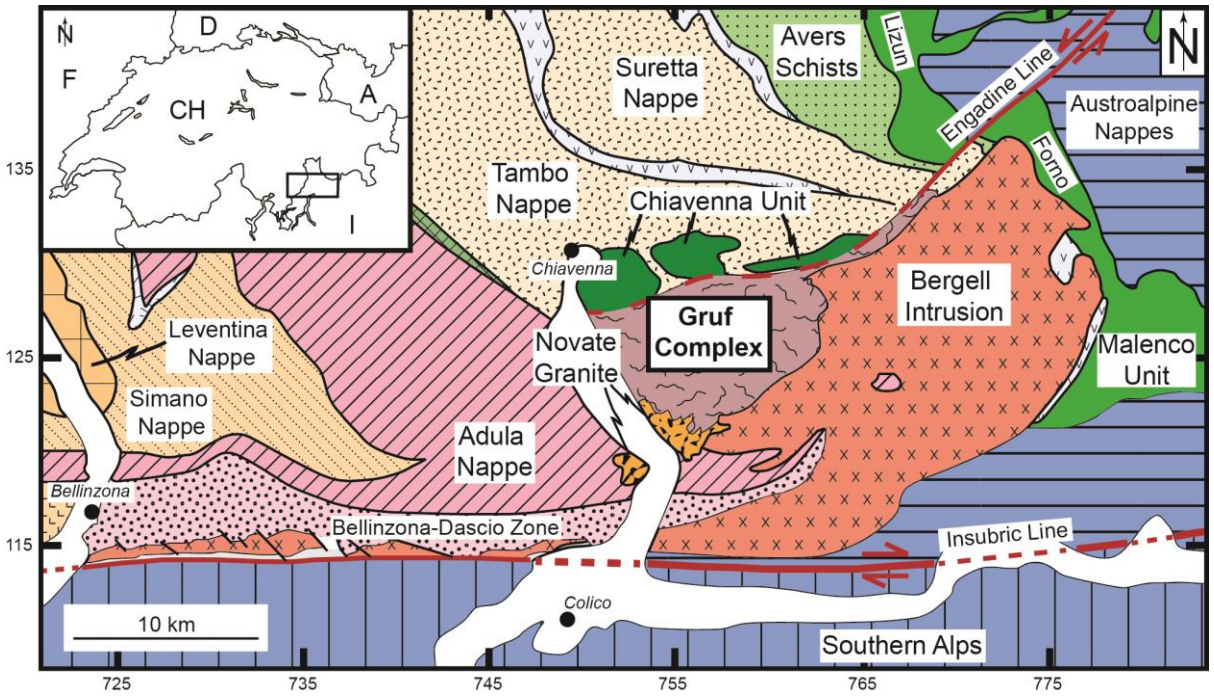

FIGURE 1 Tectonic map of the Central Alps modified after Trommsdorff and Nievergelt (1983). Coordinates are given according to the Swiss geographical grid (units in kilometres).

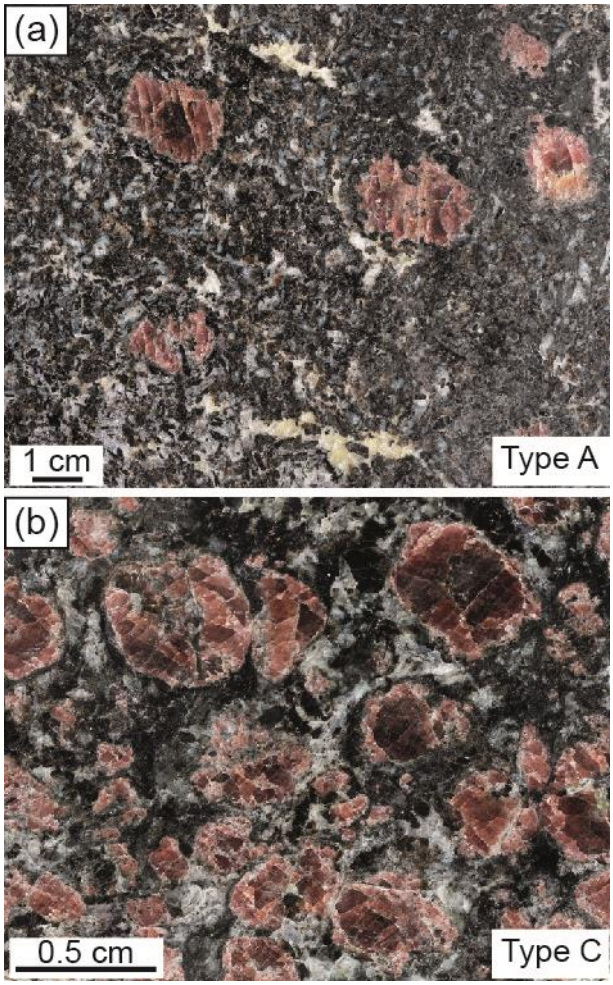

FIGURE 2 UHT granulites from the Gruf Complex. (a) Massive sapphirine-orthopyroxene-cordierite-garnet granulite (Type A) and (b) massive orthopyroxene-cordierite-garnet granulite (Type C).

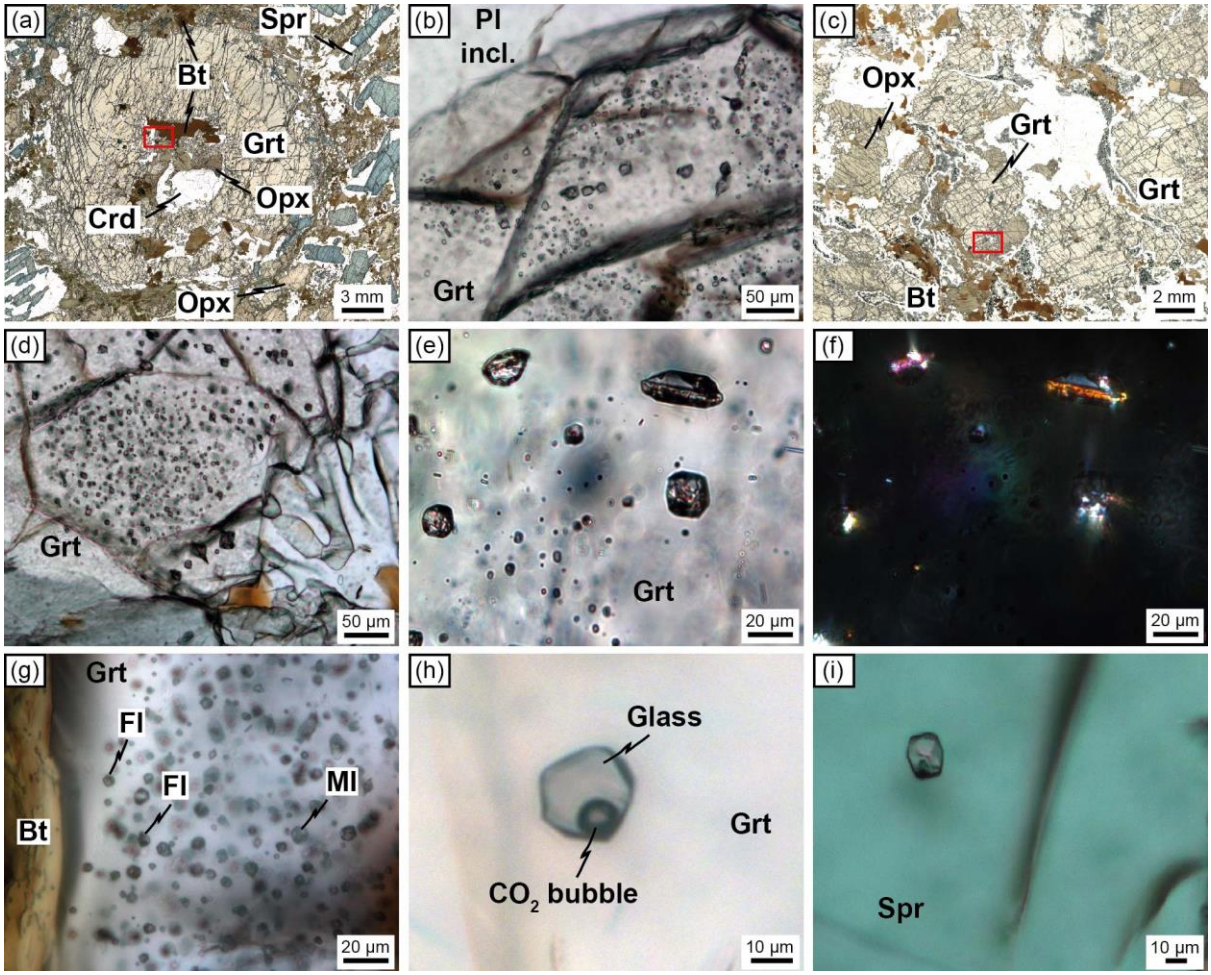

FIGURE 3 Photomicrographs of the granulites from the Gruf Complex. (a) Garnet porphyroblast from a Type A granulite showing a cluster of MI near to the core of the crystal (red box). (b) Zoom of the same cluster of MI as in (a). (c) Garnet porphyroblasts from a Type C granulite. The red box at the rim of the garnet indicate a cluster of MI. (d) Zoom of the same cluster of MI as in (c). (d) Plane-polarized light photomicrograph of MI in garnet. (e) Same as (d) under crossed-polarized light, showing multiple birefringent phases within the inclusions. (g) Fluid inclusions (FI) and MI within a cluster. (h) Glassy MI containing a CO_2 shrinkage bubble. (i) MI in a sapphirine porphyroblast from a Type A granulite.

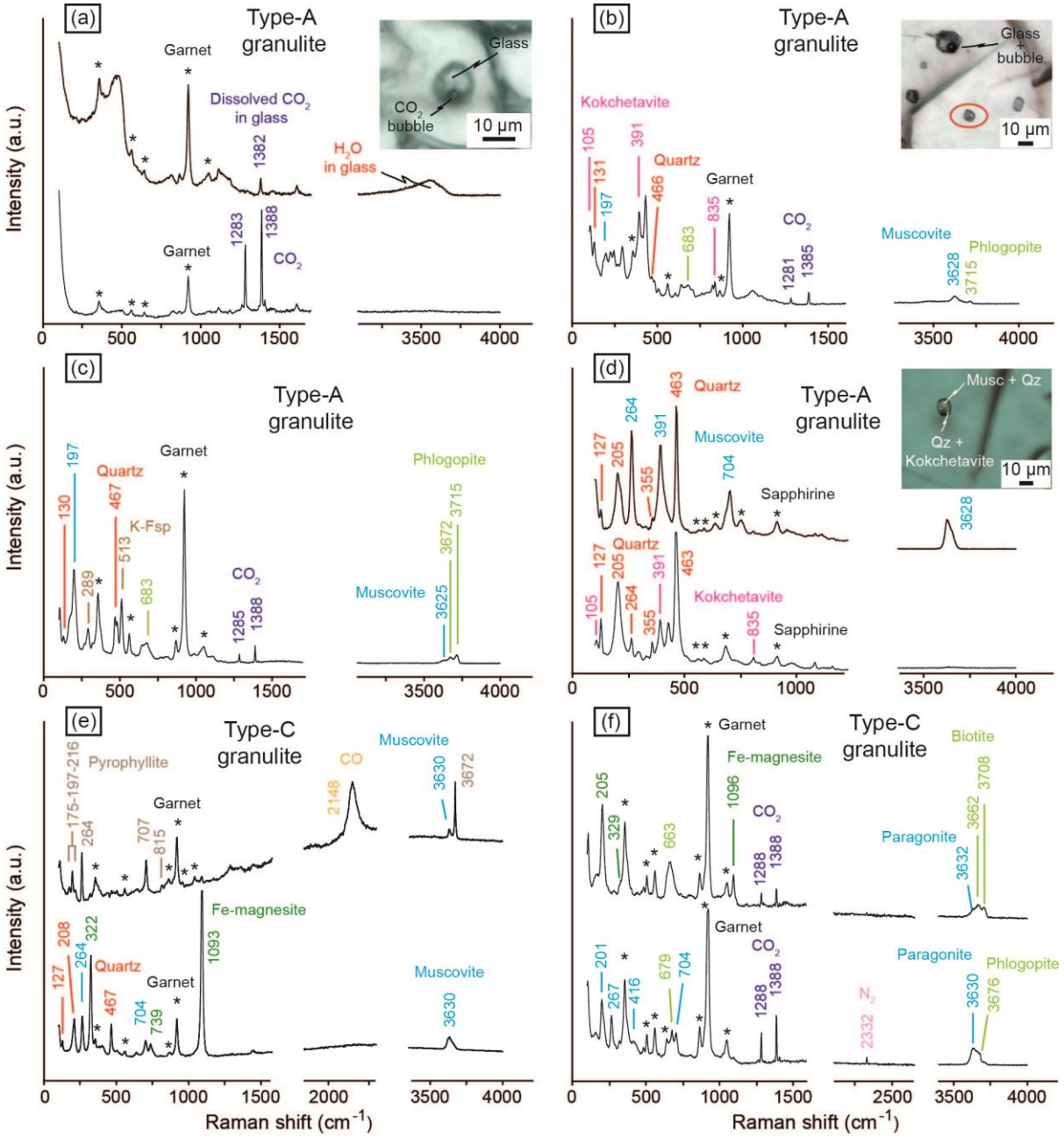

FIGURE 4 Raman spectra of nanogranitoids and glassy MI. (a) Glassy MI with a shrinkage bubble containing CO_2. (b) Analysis of a nanogranitoid inclusion (red circle) close to a glassy MI showing a shrinkage bubble. (c) Nanogranitoid with a CO_2 bubble. (d) Nanogranitoid in sapphirine. (e) Mixed inclusion (fluid + melt) showing CO together with phyllosilicates, quartz and Fe-magnesite. (f) Mixed inclusion with phyllosilicates, Fe-magnesite, CO_2 and N_2.

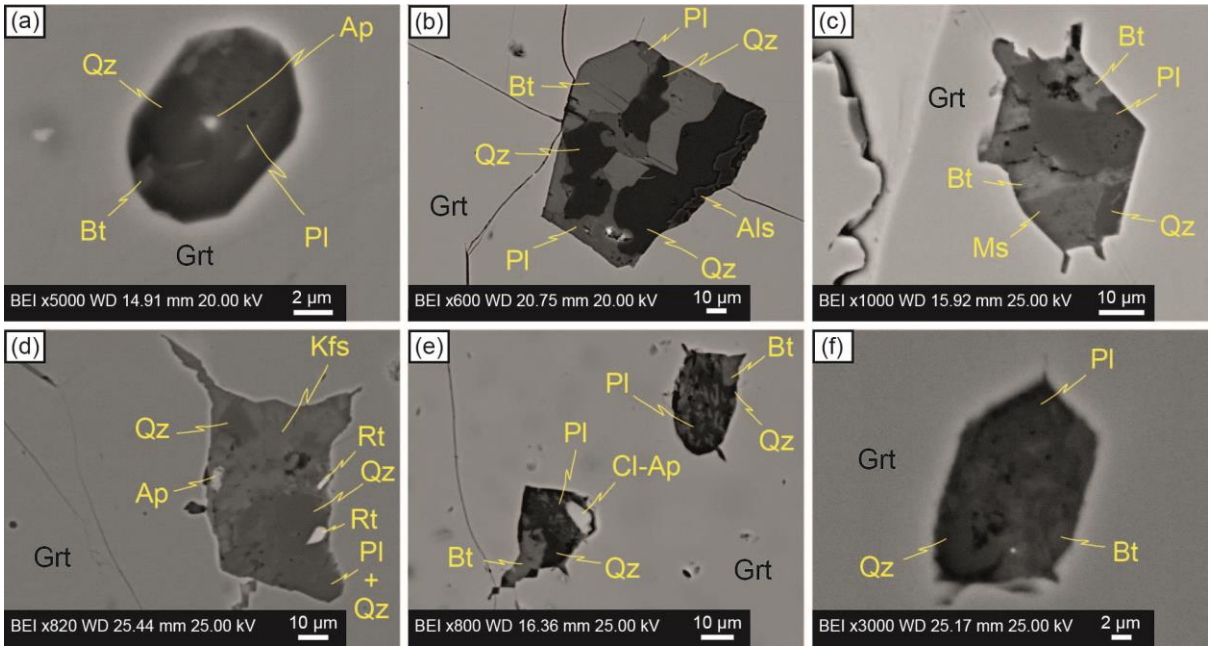

FIGURE 5 Backscattered images of nanogranitoids. Nanogranitoids from Type A (a-d) and from Type C (e-f) granulites are shown.

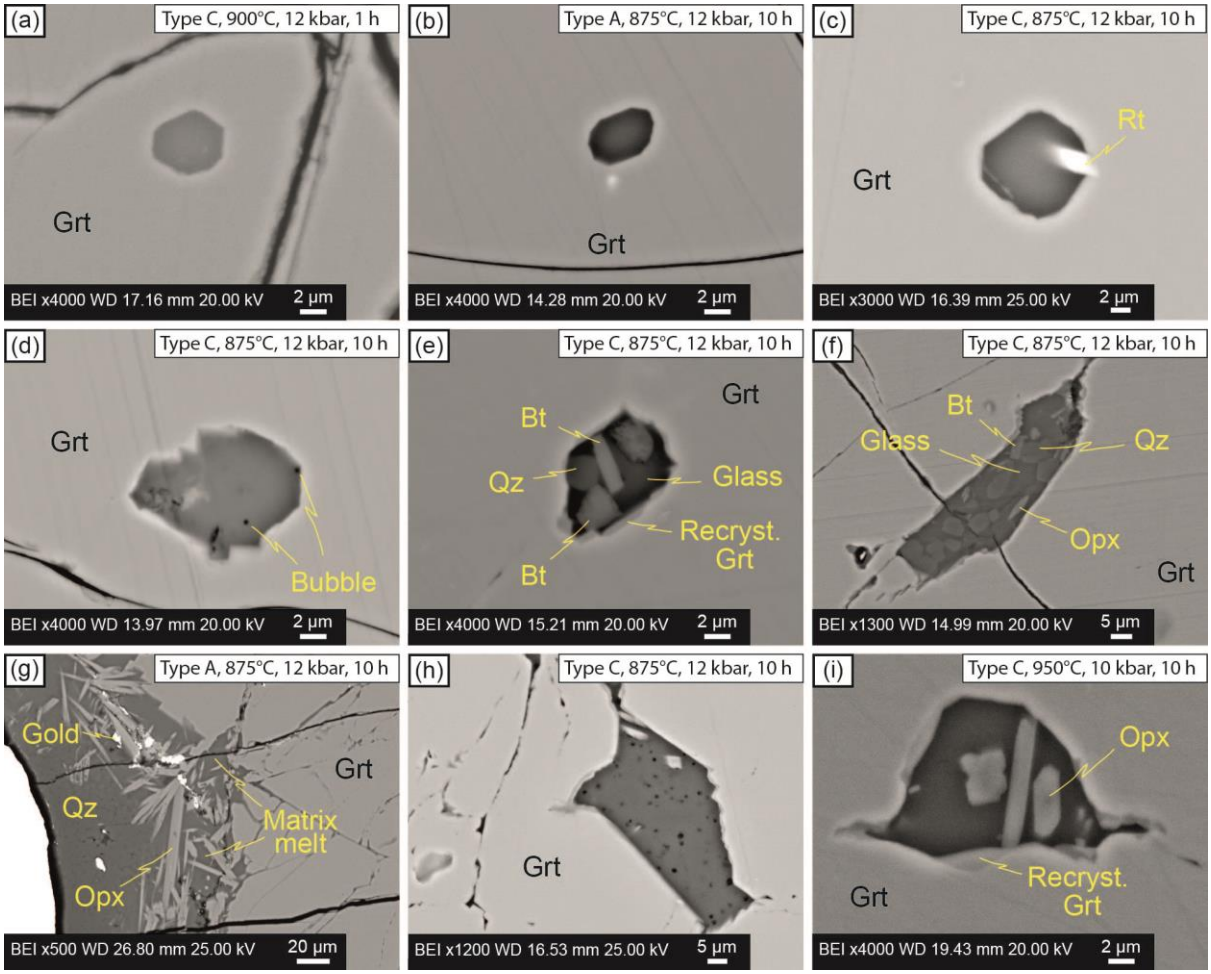

FIGURE 6 Backscattered images of experimentally remelted nanogranitoids. (a,b) Remelted MI with a well-developed negative shape. (c) Re-homogenized MI showing a trapped rutile needle, indenting the wall of the inclusion. (d) MI showing an irregular border and bubbles within the glass. (e,f) Partially remelted nanogranitoids, displaying daughter phases (biotite and quartz) and evidence of minor overheating (recrystallization of garnet and peritectic orthopyroxene). (g) Interaction of matrix melt with a garnet chip, forming peritectic orthopyroxene needles. (h) Melt pocket of infiltrated matrix melt within the garnet chip. The glass displays abundant bubbles. (i) MI from an experiment at 950 °C showing strong evidence of overheating (formation of peritectic orthopyroxene and recrystallization of new garnet at the wall of the inclusion).

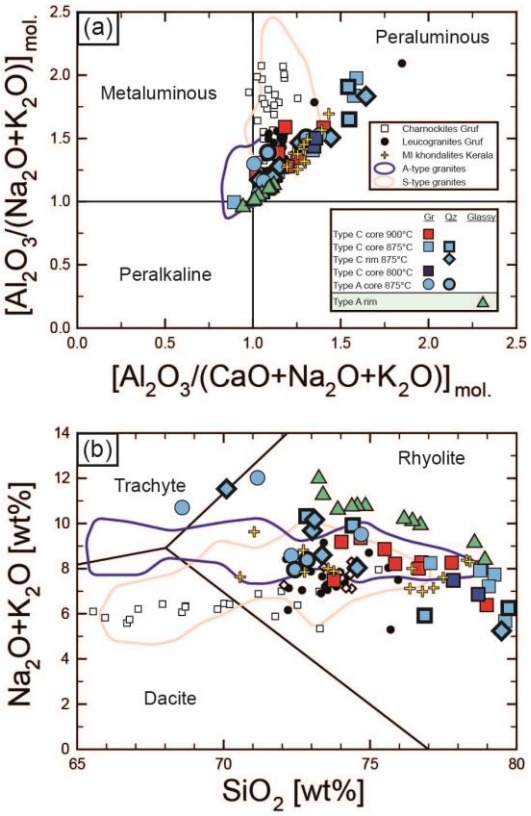

71

72 **FIGURE 7** Chemical classification of remelted and glassy MI from the Gruf Complex
73 (normalized to 100% on anhydrous basis). Reported are MI analyses of re-melting
74 experiments between 800 and 900 °C with graphite-bearing (Gr) and quartz-bearing (Qz)
75 capsules. (a) Aluminum saturation index vs. alkalinity index. (b) TAS diagram. Analyses for
76 charnockites and leucogranites from the Gruf Complex are from Galli et al. (2013), whereas
77 MI analyses from the Kerala Khondalite Belt are from Cesare et al. (2009) and Ferrero et al.
78 (2012). Data for S-type granites (Chappel & White, 1992; Jung, Hoernes, & Mezger, 2000;
79 Kalsbeek, Jepsen, & Jones, 2001; Tulloch, Ramezani, Kimbrough, Faure, & Allibone, 2009;
80 Visonà & Lombardo, 2002) and for A-type granites (Castro et al., 2012; de Almeida, de
81 Pinho Guimarães, & da Silva Filho, 2002; Florisbal, de Fátima Bitencourt, Nardi, &
82 Conceição, 2009; Ghani et al., 2014; Goodenough, Upton, & Ellam, 2000; King, White,
83 Chappell, & Allen, 1997; King, Chappell, Allen, & White, 2001; McDermott, Harris, &
84 Hawkesworth, 2000; Whalen, Currie, & Chappell, 1987; Zhang et al., 2007) are also reported
85 for comparison.

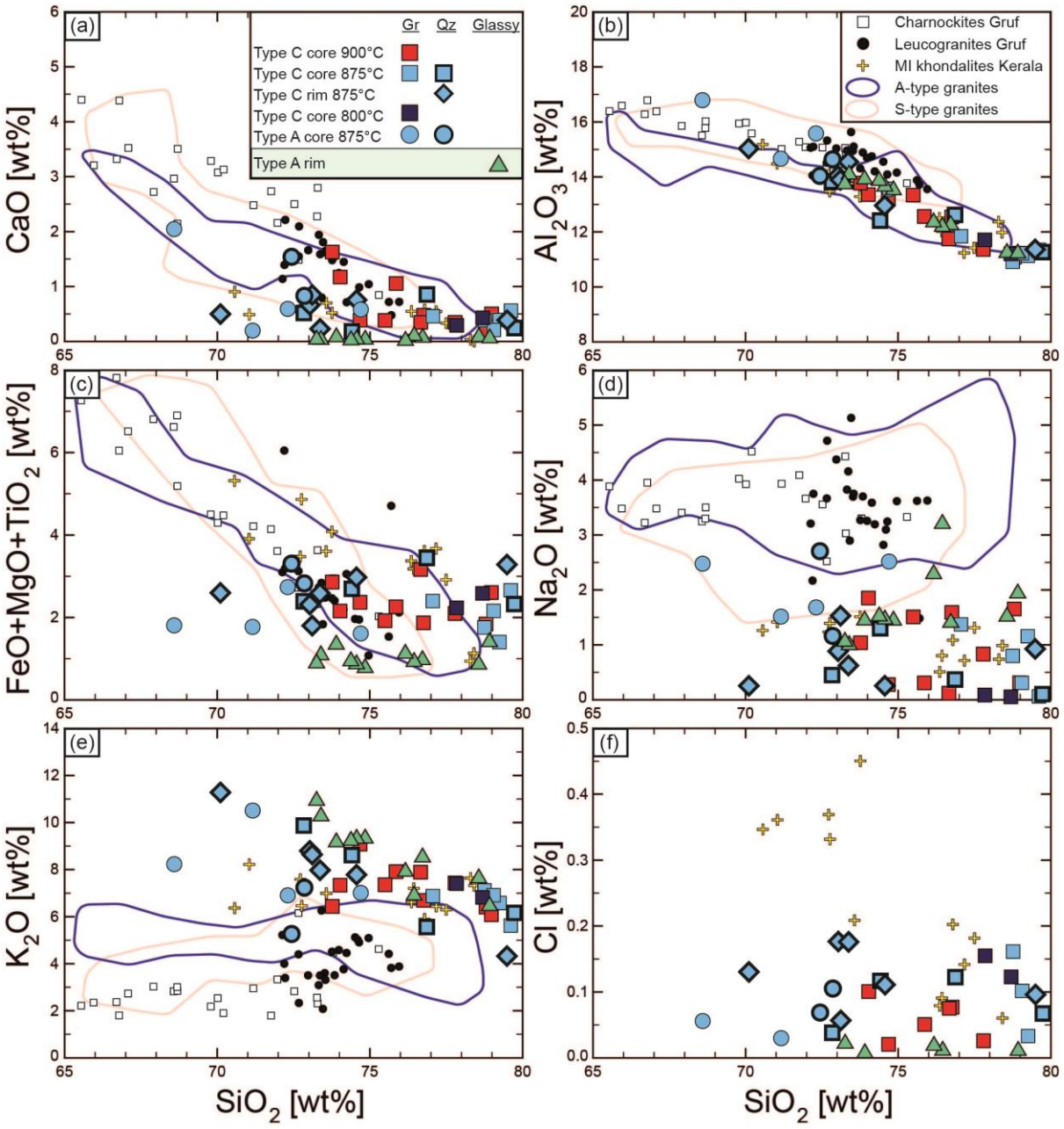

FIGURE 8 Chemical composition of glasses from experimentally remelted and natural glassy inclusions (normalized to 100% on anhydrous basis). Reference analyses are the same as in Figure 7.

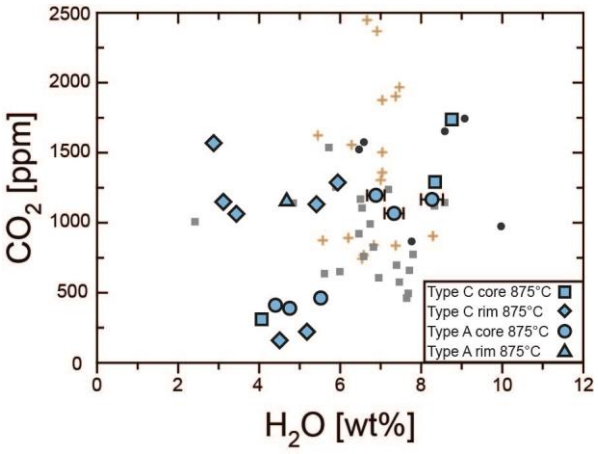

FIGURE 9 H_2O and CO_2 content measured in remelted nanogranitoid inclusions. Error bars are displayed only when bigger than the symbol. Data for MI from the Ivrea Zone (Carvalho et al. 2019) are also reported for comparison (black dots = upper amphibolite facies, grey squares = transition zone, brown crosses = granulite facies).

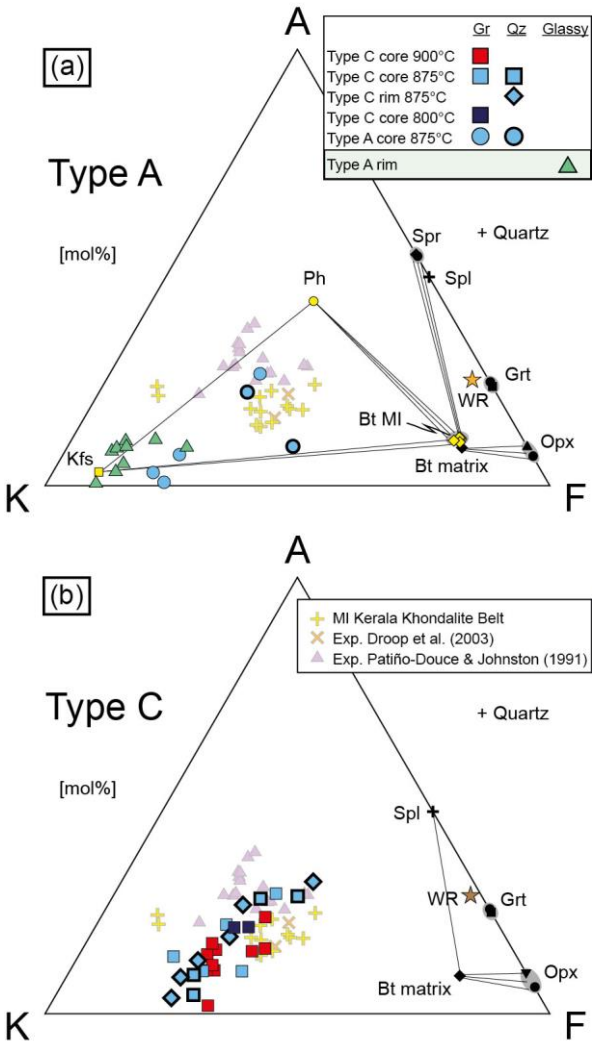

FIGURE 10 AKF diagram (after Vielzeuf & Holloway,1988) projected from quartz for MI and bulk rocks. (a) Type A granulite. (b) Type C granulite. Also reported for comparison are: melt inclusions from the Kerala Khondalite Belt (Cesare et al. 2009; Ferrero et al. 2012), experimental glasses (900 °C, 5 kbar) of Droop et al. (2003) and experimental glasses (875-1075 °C, 7-13 kbar) of Patiño-Douce & Johnston (1991).

FIGURES FOR THE ELECTRONIC APPENDIX

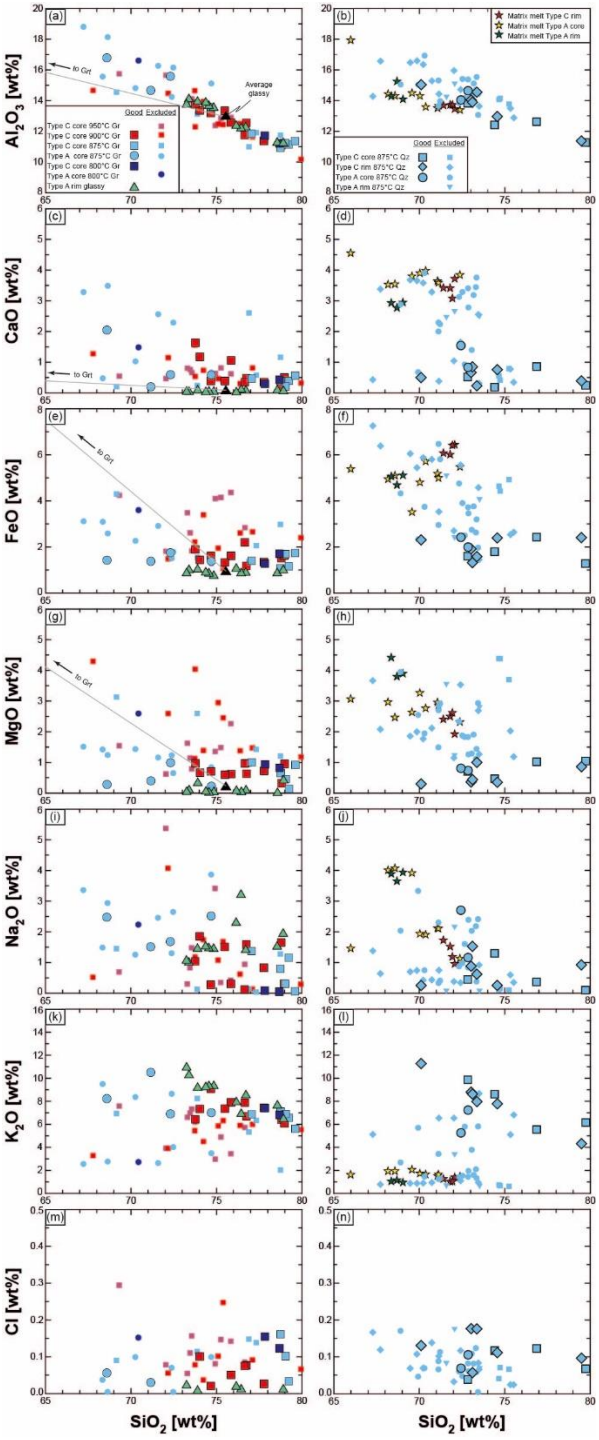

FIGURE S1 Harker diagrams showing the complete set of MI analyses. Small symbols represent disregarded analyses. The line displayed for Al_2O_3, FeO and and MgO represents the tie-line between the host garnet (Type A granulite) and the average composition of the glassy inclusions (black triangle).

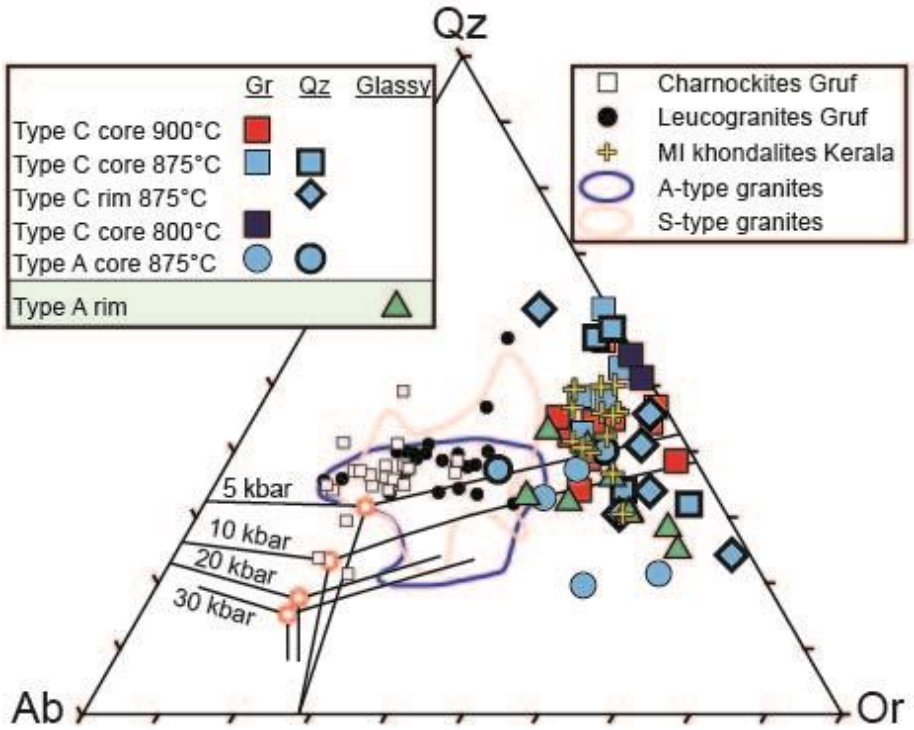

FIGURE S2 CIPW Qz-Ab-Or diagram showing normative compositions for the analysed MI and other reference analyses from the literature (see text).

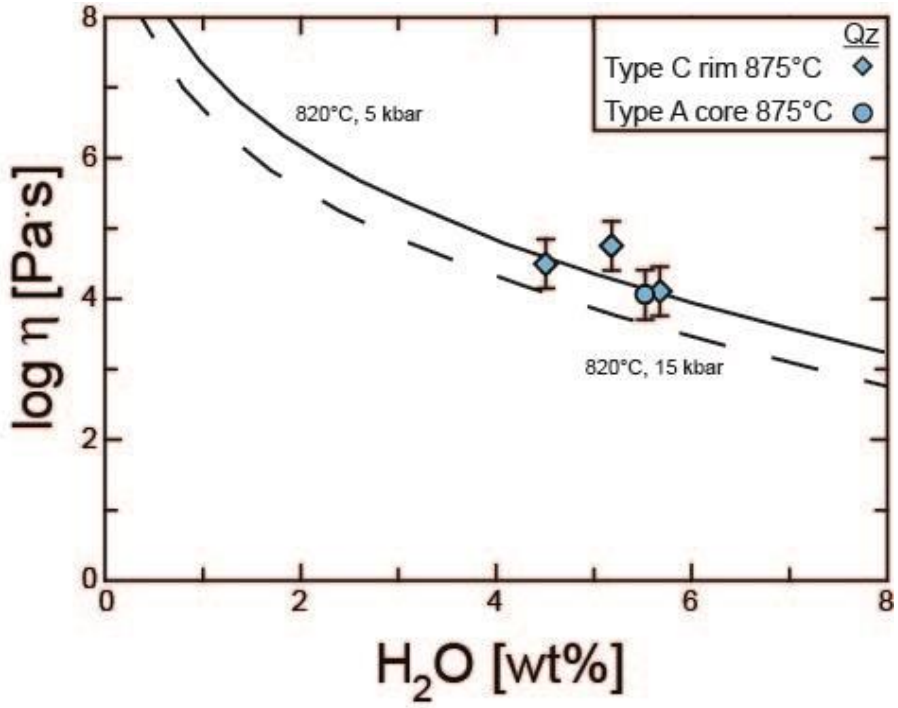

138

139 **FIGURE S3** Viscosities of rhyolitic melts vs. H_2O content (modified after Ardia et al.,
140 2008). Viscosities for MI are calculated according to Giordano et al. (2008).

141

142

143

144

145